Deanship of Graduate Studies
Al-Quds University

Magnesium Oxide Encapsulated Palladium Nano-catalysts Decorated Electrodes for Microbial Fuel Cells

Riham Waleed Muhammad Muzaffar

M.Sc. Thesis

Jerusalem – Palestine

1438 / 2017

Magnesium Oxide Encapsulated Palladium Nano-catalysts Decorated Electrodes for Microbial Fuel Cells

Prepared by:

Riham Waleed Muhammad Muzaffar

B.Sc. Materials Engineering. Al-Quds University-Palestine

Supervisor: Prof. Mukhles Sowwan

A thesis Submitted in Partial fulfillment of requirements for the degree of Master of Applied and Industrial Technology, Al- Quds University.

1438 / 2017

Al-Quds University

Deanship of Graduate Studies

Applied and Industrial Technology Program

Thesis Approval

Magnesium Oxide Encapsulated Palladium Nano-catalysts Decorated Electrodes for Microbial Fuel Cells

Prepared by: Riham Waleed Muhammad Muzaffar

Registration No.: 21312410

Supervisor: Prof. Mukhles Sowwan

Master thesis submitted and accepted, Date: 31/7/2017

The names and signatures of the examining committee members are as follows:

1-Head of Committee: Dr. Mukhles Sowwan Signature _____

2-Internal Examiner: Dr. Mousa Abu Tair Signature _____

3-External Examiner: Dr. Jamal Ghabboun Signature _____

Jerusalem – Palestine

1438 / 2017

Dedication

It’s my genuine gratefulness and warmest regard that I dedicate this work to Mom and Dad, my daughter, my husband, and my family.

Riham W. M. Muzaffar

Declaration

I certify that this thesis submitted for the degree of Master is the result of my own research, except where otherwise acknowledged, and that this thesis (or any part of the same) has not been submitted for a higher degree to any other university or institution.

Signed:

Riham Waleed Muhammad Muzaffar

Date: 31/7/2017

ACKNOWLEDGEMENT

I would first like to sincerely thank and appreciate my supervisor Prof. Mukhles Sowwan for supporting me throughout this research project. He consistently allowed this thesis to be my own work, but steered me in the right direction whenever he thought I needed it.

I would also like to acknowledge the researchers at Okinawa Institute of Science and Technology Graduate University: Vidya Singh, Cathal Cassidy, David Simpson, Sushant Kumar, Kengo Aranishi and Jeong-Hwan Kim for their passionate participation and hard work.

I would also like to acknowledge Dr. Vidya Singh for reading my thesis. I am gratefully indebted to him for his very helpful and valuable comments on this thesis.

I am also grateful to my colleagues in the Nanotechnology Research Laboratory at Al Quds University Maryam Faroun and Lena Qawasmi for their help and support.

Finally, I must express my very profound gratitude to my parents (Reem and Waleed), to my husband (Issa Qawasmi), to my daughter (Nisan) and to my sisters and brother (Salam, Aya and Muhammad) for providing me the unlimited and unstoppable support and continuous encouragement throughout my years of study and research. This accomplishment would not have been possible without them. Thank you.

Abstract

In this study, we designed and synthesized novel magnesium oxide (MgO) encapsulated palladium (Pd) nanocatalysts for decorating microbial fuel cell electrodes via the physical vapor deposition combined with gas aggregation method. This technique enabled the growth of MgO-Pd nanoparticles having the core-shell nanostructure in a controlled manner. The synthesized nanoparticles were size selected using an in-situ quadrupole mass filter, which resulted in a narrow size distribution as the average diameter for the produced MgO-Pd core-shell nanoparticles was 9 nm. Bare Pd nanoparticles with 2.5 and 5 nm average diameters were also synthesized.

The nanoparticles were directly deposited onto graphite substrates working as MFC cathodes and their performance or power output was examined by recording current production with time. It was found that the surface modification of MFC cathodes using core-shell MgO-Pd and conventional Pd nanocatalysts resulted in MFC power generation 4.67 and 4.5 times better than that produced by undecorated cathodes, respectively.

Morphological and topographical characterization of these nanoparticles were accomplished using the scanning electron microscope, the atomic force microscope and the transmission electron microscope techniques. Results confirmed the size selection data obtained by the quadrupole mass filter. Moreover, a well defined core-shell or metal oxide encapsulated structure was also revealed. Surface and structural analysis were also performed using the X-ray photoelectron spectroscopy and the grazing incidence X-ray diffraction indicating the presence of the MgO and metallic Pd before and after MFC running.

Table of Contents

List of Figures

Definitions

MFC	Microbial Fuel Cell
MgO	Magnesium Oxide
Pd	Palladium
PVD-GA	Physical Vapor Deposition combined with Gas Aggregation
QMF	Quadrupole Mass Filter
UHV	Ultrahigh Vacuum
SEM	Scanning Electron Microscope
TEM	Transmission Electron Microscope
AFM	Atomic Force Microscope
PEM	Proton-exchange membrane
COD	Chemical Oxygen Demand
XRD	X-ray Diffraction
GI-XRD	Grazing Incidence XRD

Chapter One

Introduction

Why is something so small so big? The answer comes with nanotechnology.

Size matters and that's a fact. It's nanotechnology that affords us the chance to construct and deal with uncommon nanostructures, nanodevices and nanotools that are on the size scale of a molecule (Leary, 2010) , leading to revolutionary developments and researches in a very wide range of fields which give the birth of various novel applications and designs.

The most common overly simplistic definition of nanotechnology relies on the size range of the built structure or particle, which has a limit of about 100 nm. However, this size limit isn't a highly agreed-upon value (Leary, 2010). The most distinctive and important feature of these nanostructures is that they have characteristics that are quite different to the corresponding bulk materials (Cassidy et al., 2013), which can be related to not only the nanoscopic scale and subsequent increased surface area, but also the way the atoms or constituents of the nanostructure are assembled and organized (Leary, 2010).

The ability of changing the particle size makes it possible to design new nanoparticles with different and remarkable catalytic, optical, magnetic, electrical and thermal properties, which endow these nanoparticles with potential applications and technological advancements for many years in many electrical and optical devices, solid dielectric materials, nano-biomaterials, high thermal conductivity nanofluids (Gracia-Pinilla et al., 2010), microbial electrochemical cells such as microbial electrolysis cells (MECs) and microbial fuel cells (MFCs) (Fan et al., 2011).

Microbial fuel cell (MFC) technology is a prospective technology that has been intensively studied in the recent decade, because it offers a solution for environmental sustainability by simultaneously producing renewable energy and removing pollutants (Wang et al., 2015). They are also very promising for wastewater treatment, biotransformation and biosensors (Fan et al., 2011). Hence, researchers believe that MFCs may in the future solve the big problems of the worsening environment and rapidly depleting natural resources (Qiao et al., 2011).

It's known that significant amounts of energy can be found in organic matter such as carbohydrates, which can be found in agricultural and municipal waste. MFC as a bio-electrochemical system (BES) can directly convert the chemical energy stored in the organic compound into electrical energy via microbial metabolism (Alatraktchi et al., 2012) with advantages of low maintenance, environmentally friendliness, high conversion efficiency, ambient and low operating temperatures (Wen et al., 2013). Besides, the produced electrical current can be utilized in many other functions, including producing value-added chemicals such as H_2 in microbial electrolysis cells (MECs) or driving water desalination in microbial desalination cells (MDCs) (Wang et al., 2015).

In the MFC's anode chamber, bacteria grow in a solution by oxidizing organic matter (catalyze fuel oxidation), which subsequently results in releasing electrons and protons that react in the cathode chamber to produce water. Electricity is generated when the electrons travel between the chambers through an external circuit (Alatraktchi et al., 2014). The efficient anode electrode should have excellent conductivity for electron transfer and good biocompatibility for microbial inoculum, growth and adhesion (Wen et al., 2013). Actually , the development of sturdy, cheap and highly efficient electrodes is

highly desired in the recent years because the cell electrode is the key component in deciding the performance and cost of MFCs (Wei et al., 2011; Logan, 2010).

Thus, obtaining optimum performance of MFC requires engineering of a novel electrode design and control over many variables and parameters such as electrode material which affects electron transfer, bacterial attachment and substrate oxidation (Alatraktchi et al., 2012), electrode's surface area and surface roughness (optimal pore structure), cost, durability and the catalytic behavior of the used bacteria and/or nanocatalysts because they can affect and control the efficiency of the electrode, which necessarily determine the extent to which the MFC system is scaled up (Wen et al., 2013).

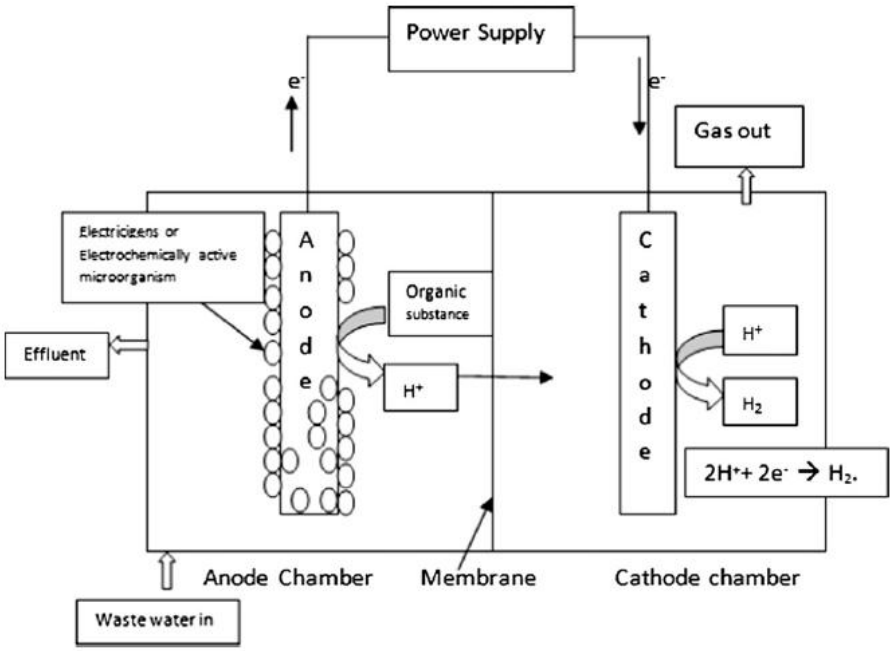

Figure 1.1: Schematic diagram of MFC *(Kundu et al., 2012)*

Electrodes can be classified ,according to whether or not the bacteria is used as a catalyst, into two main categories; bio-electrodes (including anode and bio-cathode) and chemical electrodes (classified into air-cathode and aqueous air-cathode) (Wei et al., 2011).

Although both anode and cathode contribute to the cell efficiency, the cathode itself is actually the most challenging aspect of the MFC design due to the need to have a three-phase interface: air (oxygen), water (protons) and solid (electricity) (Logan, 2010).

Recently, studying electrode material and its configuration has gained an increasing interest in investigating MFCs. Over the past decade, many electrodes have been tested for performance in MFCs. In general, for all MFC electrodes, the electrode base material should have good conduction, long term stability, high mechanical strength and low cost. Currently the most widely used based materials are carbon materials such as carbon paper and non-corrosive metals as they manifest the previously mentioned general characteristics. (Wei et al., 2011)

Increasing the electrode's surface area results in more space for bacteria to cling to the surface and more efficient current collection (decreased transfer resistance of electrons and higher conductivity), which consequently lead to increase the MFC generated electricity (Wei et al.,2011). Therefore, researchers recently tend to develop electrodes decorated with nanostructures because surface modification utilizing nanotechnology can provide a unique opportunity to increase the electrode's efficiency due to the distinguished features and properties of nanomaterials such as nanoparticles and carbon nanotubes (Fan et al., 2011). The improved electron transfer is actually because the use of nanocatalysts can cause shorter charge diffusion lengths, higher diffusion rates along grain boundaries and less or relived mass transfer limitation of substrates, leading to better MFC performance and improved power output. In Fact, nanomodification of MFC electrodes can help in extending the electrode and the whole cell lifetime, which is an essential requirement for obtaining a scalable MFC (Alatraktchi et al., 2012).

However, the most challenging side in designing the MFC is to bring this technology out of laboratory and engineer practical systems to be used for industry and in real-world applications at larger scale production (Logan, 2010), which necessarily requires MFCs with high energy conversion efficiency and low cost (Qiao et al., 2011). But sometimes MFCs may not be performing well due to energy conversion losses and subsequently less power output, so it's highly recommended to avoid, reduce or control these losses, which may be induced due to slow electrode kinetics, poor mass transport and high ohmic resistance (Qiao et al., 2011; Wang et al., 2015).

Electrode kinetics is a complicated catalytic process which involves certain electrochemical reactions (oxidation / reduction) to transfer electrons at an electrode/electrolyte interface. This explains why using a good electrode is necessary to aid faster electron transfer as these reactions become more reversible and subsequently reducing the activation overpotential. The mass transport loss is mainly caused by concentration polarization, that usually occurs at high current densities under diffusion control resulting in high overpotentials. Thus, porous electrodes with optimal pore structure and pore distribution should be used as they are able to provide high specific surface areas, which is beneficial to the mass transport. As for the Ohmic loss, it can occur due to high ohmic resistance of the cell components and interconnects so it's important to use a conductive electrode and insure good connections (Qiao et al., 2011)

Some examples of the investigated nano-catalysts in MFCs ,that have proven to display superior catalytic behavior especially when compared with conventional catalysts, are metallic nano-particles, nano-rods, nano-wires and nano-engineered bimetallic/trimetallic catalysts (Qiao et al., 2011). However, size, shape, chemical composition, density, phase

properties and dispersion uniformity of the used metallic NPs can significantly affect their catalytic activity (Fan, et al., 2011; Qiao et al., 2011).

Ma et al. prepared nanocomposites of iron oxide and partly graphitized carbon as a cathode catalyst for MFCs. They found that the Fe_3O_4/PGC composites are highly efficient with low cost catalysts for MFCs and that they exhibit high oxygen reduction reactivity, low charge transfer resistance, and long-term stability (Ma et al., 2014).

Alatraktchi and coworkers decorated silicium electrodes with Ti and Au nanograss. They found that the maximum power density achieved by the plain silicium was only 0.002 mW/m^2 , while depositing Ti and Au nanograss on one side generated a maximum power density of 2.5 mW/m^2 and deposition on both sides gave 86.0 mW/m^2. Furthermore, the use of carbon-paper electrodes with deposited Au nanoparticles only on one side generated maximum stable power density of 346.9 mW/m^2, which is 2.9 times higher than that achieved by the plain carbon-paper (Alatraktchi et al., 2012).

In another work for Alatraktchi et al., carbon paper electrodes for MFC were coated with layers of different densities of gold nanoparticles using physical vapor deposition (sputtering) method; to study the effect of the amount (density or coverage) of NPs used for decoration on microbial community and MFC performance. They found that by depositing carbon paper electrodes with Au NPs of 50 nm and 100 nm layer thickness on one side, respectively, the maximum achieved power densities were 1.22 and 1.88 times higher than that obtained with the control electrode. Also, more diverse bacterial communities were found with higher Au NP densities (Alatraktchi et al., 2014).

Xu et al. used Fe nanoparticle-modified graphite disks as anodes for MFC and hereby achieved average current density up to 5.89-fold higher than that generated by the plain graphite anodes (Xu et al., 2012).

In another study by Fan et al., Au nanoparticles decorated anodes for multi-anode microbial electrolysis cell produced current densities up to 20-fold higher the plain graphite anodes by Shewanella oneidensis MR-1, while Pd-decorated anodes produced 50-150% higher than the control (Fan et al., 2011).

Moreover, Sharma and coworkers decorated carbon paper electrodes with Pt for an *E.coli*-based microbial fuel cell which gave a 6-fold increase in power density (Sharma et al., 2008).

NPs composed by two or more metals in a core-shell structure are attractive for a variety of applications such as catalysis, optoelectronic devices and biomedicine. These hybrid nanoparticles are considered a promising type of catalysts, in the field of heterogeneous catalysis, because they can possess a unique combination of improved chemical and physical properties resulting from the interaction of the different constituents. They also can perform more than one function at a time. The integration of two or more metals in one nanoparticle is therefore highly desirable (Mayoral et al., 2010; Mayoral et al., 2012; Singh et al., 2014).

Furthermore, some of the interesting benefits of the core-shell structures are their ability to reduce the precious metals loading such as Pt and Pd (cost-efficiency) and providing the core a kind of support so they won't lose their catalytic activity (stability) or at least it will be maintained for longer time (durability) (Qiao et al., 2011).

For fuel reactions particularly, core-shell structured NPs are the most favorite catalysts; since the control of the size, shape, composition and phase properties of them is much easier than other nanostructures. Moreover, many core-shell metallic NPs exhibit improved catalytic activity. For example, Ni@Pd core-shell nanoparticles supported on multi-walled carbon nanotube, in an alkaline medium, increase the electrocatalytic activity and stability considerably towards methanol oxidation compared with PdNi/MWCNTs and Pd/MWCNTs. In comparison with Pd nanoparticles and hollow Au nanospheres, the hollow Au@Pd core-shell nanostructure with a raspberry surface possesses superior electrocatalytic properties towards oxidation of methanol, ethanol and formic acid in alkaline media (Qiao et al., 2011).

In this study, decorated graphite electrodes with metal NPs have been used in the designed MFC. The used nanocatalysts were magnesium oxide encapsulated palladium NPs (MgO-Pd core-shell nanostructures) and conventional Pd NPs; in order to study and investigate the effect of metal oxide encapsulation or the core-shell structure on the performance of the electrodes and the whole MFC.

In General, nobel metal nanoparticles, such as silver, platinum, gold and palladium, exhibit outstanding and unique set of physical, chemical, optical and thermo dynamical properties, making them ideal to use in many applications such as catalysis, sensors, magnetic recordings, biotechnology, as well as drug delivery. Particularly, because of their high surface to volume ratio, palladium NPs are extensively used in heterogeneous and homogeneous catalysis. Pd is actually a well-established catalyst material especially when supported on carbon substrates because of its outstanding activity and selectivity for a variety of reactions (Singh et al., 2015; Jin et al., 2010). Pd NPs are also useful in

areas like sensing, chemo-optical transducers and plasmonic wave guiding as they have another important feature, which is known as the surface plasma resonance. (Petla et al., 2012)

However, The most challenging sides in synthesizing Pd NPs are the control of NP size, avoiding the agglomeration of NPs during synthesis and storage (Petla et al., 2012). Despite of Pd superior activity, it still suffers from extremely high cost, and lifetime degradation owing to coalescence and sintering and associated irreversible reduction in surface area which make the NPs less stable and may lose their stability. However, metal oxide encapsulation can be performed to address these issues. This mechanism involves metal oxide formation as a supporting shell around the Pd core, which can powerfully minimize deactivation of the catalyst caused by metal sintering. Oxide encapsulation mechanism primarily requires control over microstructure and maintenance of the high catalytic activity of the core catalyst, by appropriate choice of material set and synthesis method (Singh et al., 2015).

MgO has been frequently studied and used as a support for Pd nanocatalyst. Based on literature, it's indicated that a Pd core surrounded by an MgO shell could be formed and that MgO NPs exhibit a highly porous structure when synthesized alone from the gas-phase system, which is an important requirement in catalyst encapsulation (Singh et al., 2015).

Nanoparticles and nanoclusters can be formed through different techniques such as chemical methods, where the kinetic processes involved in the method make very likely the appearance of core-shell structures, or physical methods such as inert gas condensation, which enables the creation of diverse NPs structures with narrow size

distributions and controlled coverage. Furthermore, it allows a great control over elemental composition of the produced NPs, since it mainly depends on the composition of the target from which the materials is sputtered (Singh et al., 2015; Cassidy et al., 2013). Moreover, it avoids the inherent products introduced by chemical synthesis from precursors and surfactants (Singh et al., 2015).

Given the size effect that dominates the physics of the NP, a major feature of the physical vapor deposition combined with gas aggregation (PVD-GA) technique is the compatibility with in situ mass filter of the produced nanocluster beam (Cassidy et al., 2013). Furthermore, this method enables inexpensive, soft-landed, stable, reproducible films with low impurity levels (Singh et al., 2015). The gas-aggregated sputtering technique was originally reported by Haberland et al.,1994.

Therefore, heterogeneous gas-phase synthesis has been widely reported for the synthesis of metallic NPs. For example, Singh et al. developed a controlled gas-phase synthesis method for engineering high performance noble Pd core- MgO porous shell nanocatalysts, which were produced using multi-target gas-aggregated sputtering chamber. Their catalytic activity towards methanol electro- oxidation was examined. They found that the catalytic performance was improved relative to simple Pd NPs due to the inhibition of Pd coalescence by the metal oxide shell (Singh et al., 2015).

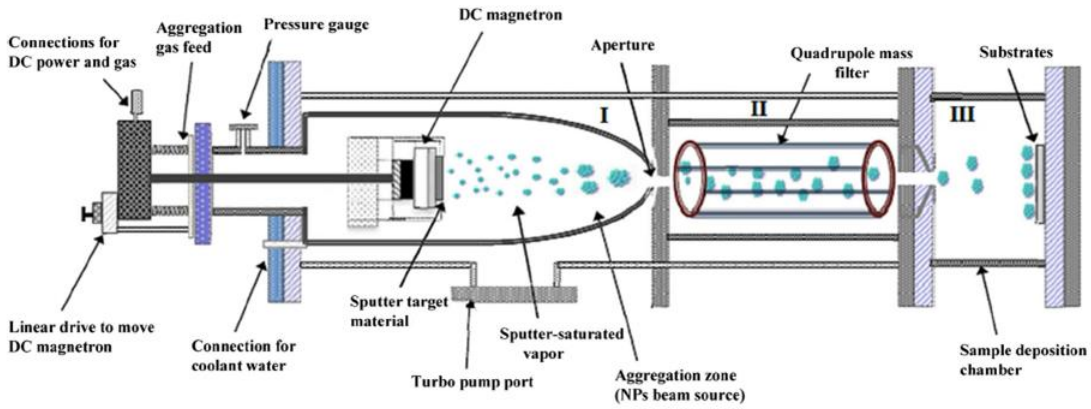

Figure 1.2: Schematic diagram of the magnetron-sputter inert-gas condensation set-up *(Singh et al., 2014)*

In another study by Singh and coworkers, silicon-silver (Si-Ag) hybrid multifunctional NPs were produced using gas-aggregated co-sputtering from elemental independent neighboring source targets. They also produced Janus and core-satellite structures by varying Si-Ag sputtering power ratio (Singh et al., 2014).

Mayoral et al. synthesized Co-Au bimetallic NPs by inert gas condensation forming initially core-shell and bimetallic crystals. However, after heating, the Co NPs changed their morphology into a fine layer forming a perfect interface with the gold as revealed after studied by a high resolution STEM (Mayoral et al., 2010).

In the current work, physical vapor deposition in combination with gas aggregation technique from Mantis Deposition Ltd (Oxon, UK) is used to decorate electrodes for microbial fuel cells. Palin and decorated graphite electrodes with simple Pd and MgO-Pd core-shell NPs were imaged using the scanning electron microscope (SEM) to examine surface morphology. Moreover, the transmission electron microscope (TEM) was used to determine the nano-particle size distribution (PSD), morphology, crystallinity and

coverage. Surface morphology and topography were investigated using atomic force microscopy (AFM, Bruker Multimode 8, Nanoscope V) in tapping mode.

Further characterization including surface and elemental analysis were also performed using X-ray photoelectron spectroscopy (XPS) and Grazing Incidence X-ray diffraction (GI-XRD). In addition, cyclic voltammetry (CV) test was performed for electrochemical analysis and testing the electrode's stability.

However, this research is actually a consequence of a previous work done by student Lena Qawasmi at OIST supervised by professor Sowwan too. But the main difference in this study is the synthesis of the novel binary or core-shell nanostructures (magnesium oxide encapsulated palladium nanoparticles) while in the previous work, electrodes were decorated using nanoislands of simple palladium and gold. More characterization techniques were also performed to get more understanding of the behavior and interaction of the decorated electrodes with the designed microbial fuel cell. However, the MFCs were designed in the same way.

Research Objective and Specific Aims

The main objective of this study is to synthesize magnesium oxide encapsulated palladium NPs in a novel design serving as nano-catalysts for decorating electrodes in microbial fuel cells to optimize the cell's power generation.

Specific aims:

- Characterization of MgO-Pd nanoparticles and studying morphology of electrodes, before and after interaction with the MFC, using several methods such as the Scanning Electron Microscopy (SEM), Transmission Electron Microscopy (TEM) and Atomic Force Microscopy (AFM).

- Spectroscopic analysis of the NPs using the X-ray Photoelectron Spectroscopy (XPS).
- Crystallographic and structural analysis of the NPs using the Grazing Incidence X-ray Diffraction technique (GI-XRD).
- Figure out all factors that may influence the MFC power generation in order to standardize and optimize the cell performance, such as the cell design (electrodes material, size and surface area, chambers, connections, separators, membrane, etc.), electrochemical properties of the used electrolyte (COD test), operating time, size of NPs, their catalytic behavior and the oxide encapsulation process. However, simple Pd NPs (without encapsulation) were also used and will be addressed.

Thesis Organization

My research passes through the following main phases, 1) nano-decoration of the graphite electrodes by depositing NPs using physical vapor deposition with gas aggregation technique, 2) characterization of these electrodes before interaction, 3) MFC assembly, 4) testing MFC performance by measuring current and calculating power, 5) characterization of electrodes after interaction, 6) analysis of the effect of surface nano-modification on the electrode's efficiency and the MFC performance.

This thesis includes four chapters; chapter one involves an introduction that clarifies the main concepts introduced in this study, introduces the general motivations, reviews some related previous works, explains the main idea and gives the reader a brief description of our work. Chapter two presents all materials and methods used to facilitate the experiments involved in this research and it also explains the physical vapor deposition with gas aggregation technique in details which is the main method used for synthesizing

and depositing the nanoparticles in this work. Chapter three displays the obtained results and discusses them. Chapter four gives a clear summary including the main conclusions and recommendations for future work.

Chapter Two

Methods and Materials

2.1 Preparation of Nanoparticles Decorated Electrodes

2.1.1 Preparation and Deposition of Size-selected Pd and MgO-Pd Nanoparticles by Physical Vapor Deposition Combined with Gas Aggregation Method

Pd and MgO-Pd nanoparticles were formed in the gas phase using sputtering and inert-gas condensation in the ultrahigh-vacuum (UHV) system. The deposition system consists of a nanocluster sputtering source, a quadrupole mass filter (QMF) and a deposition chamber (Mantis Deposition Ltd, UK). The QMF allows in-situ monitoring of particle sizes giving the mass spectrum of Pd nanoparticles as shown in Figure 3.4. For 5 nm Pd nanoparticle depositions, the magnetron power and Ar gas flow rate were set to 15 W and 70 sccm, respectively. For 2.5 nm Pd nanoparticle depositions, the magnetron power and Ar/He gas flow rate were set to 6 W and 50/10 sccm, respectively. The aggregation zone length was set to 100 mm and 40 mm for 5 nm and 2.5 nm Pd nanoparticles, respectively. During depositions of both types of Pd nanoparticle, the pressures were $\sim 6.0 \times 10^{-4}$ and $\sim 2.0 \times 10^{-1}$ mbar in the deposition chamber and in the aggregation zone, respectively. For binary Mg-Pd nanoparticle, Ar and He flow rates were 90 and 10 sccm (respectively), resulting in an aggregation zone pressure reading of 3.5×10^{-1} mbar. The aggregation zone length was set to 100 mm. The sputtering power supplied to the Pd target (30 W) and Mg target (45 W). The nanoparticles were directly deposited on carbon coated Cu/Au grids, Silicon substartes, and MFC cathodes. In order to obtain suitable substrate coverage, the deposition timeranged from a few minutes (for preliminary AFM and TEM structure

characterizations on mono-disperse nanoparticles) up to 80 minutes (for MFC cathodes). Substrate table rotation was set at 2 rpm for all depositions, to ensure uniform coverage.

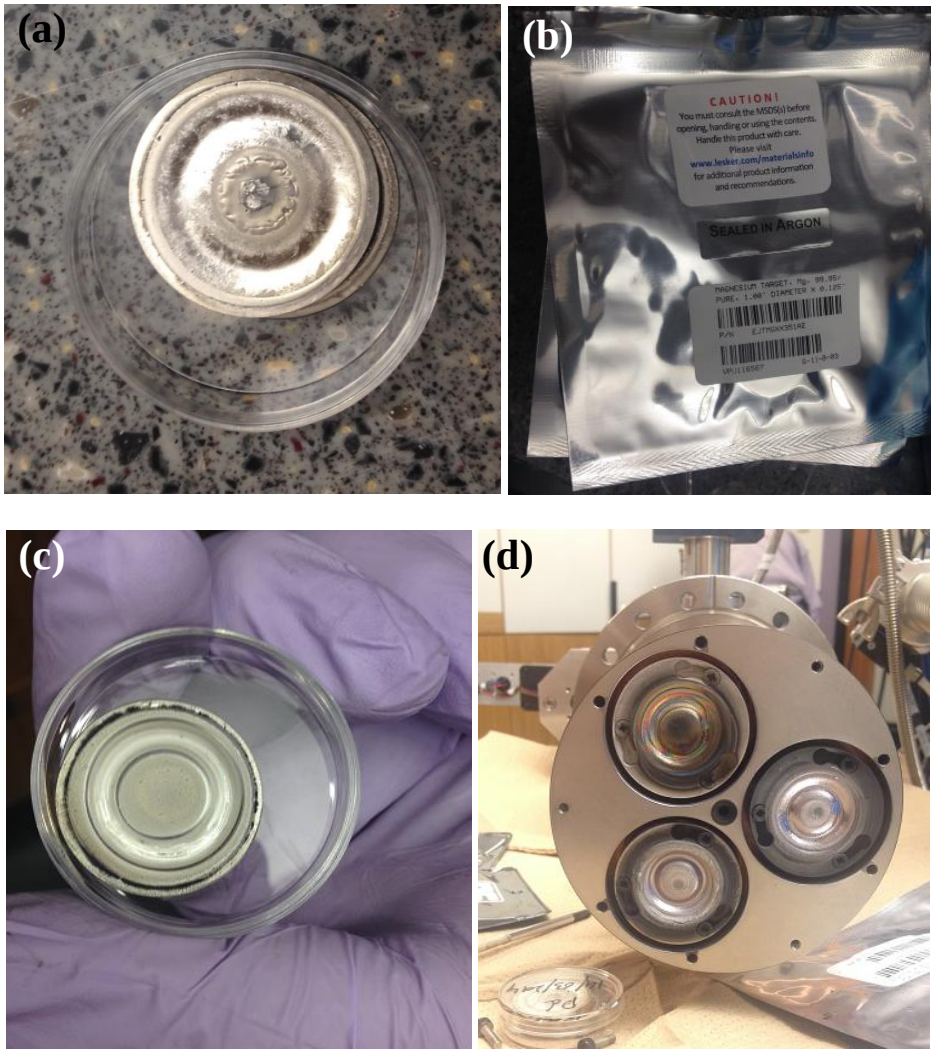

Figure 2.1: (a) and (b) Mg Target, (c) Pd Target, (d) Three independent sputter sources *"Acquired at Okinawa Institute of Science and Technology"*

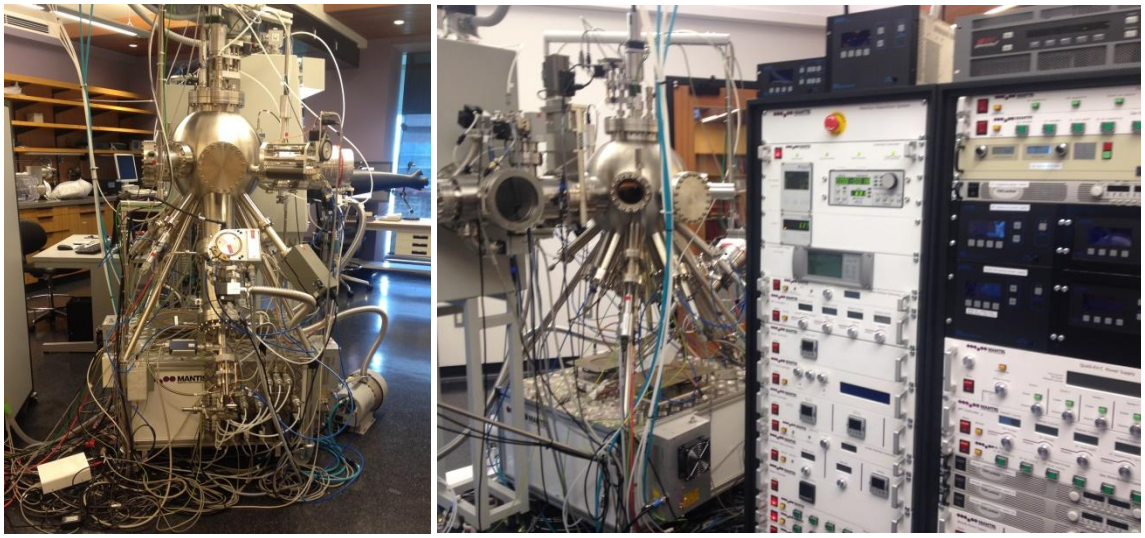

Figure2.2: Mantis deposition system *"Acquired at Okinawa Institute of Science and Technology"*

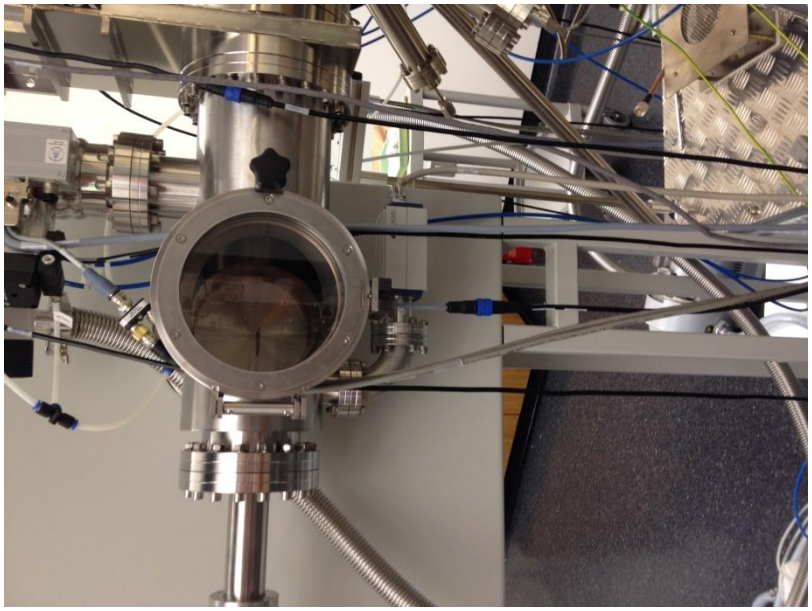

Figure 2.3: The deposition chamber in which nanoparticles are being deposited onto the substrate *"Acquired at Okinawa Institute of Science and Technology"*

2.1.2 Quadrupole Mass Filter (QMF)

The *in situ* QMF is a major component in the deposition system by Mantis, which is incorporated to facilitate the nanoparticle design, monitoring and feedback. The QMF gives live feedback on nanoparticle yield and size distribution, and how changing the process variables and parameters can affect the whole deposition process.

As the name implies, the QMF consists of four cylindrical electrodes, ideally of hyperbolic cross section, that are set parallel to each other in a radial array. This design was selected for practical as well as economic reasons. The quadrupole is the component responsible for the filtering action, which is obtained by applying a combination of a constant or time-independent (dc) and an alternating or time-dependent (ac) potentials. (Miller et al., 1986)

Charged nanoparticles passing through the quadrupole (4 biased electrodes) experience deflections to their trajectories on the basis of their mass-to-charge ratio (*m/z*); only clusters with a certain *m/z* have a stable trajectory through the potential gradients, and are deposited onto the substrate. So, NPs are filtered within the QMF as a result of their deflections depending on their mass-to-charge ratio, which indicates that the electrical charge on the cluster is a prime parameter upon which the mass analysis and the entire process rely. (Cassidy et al., 2013)

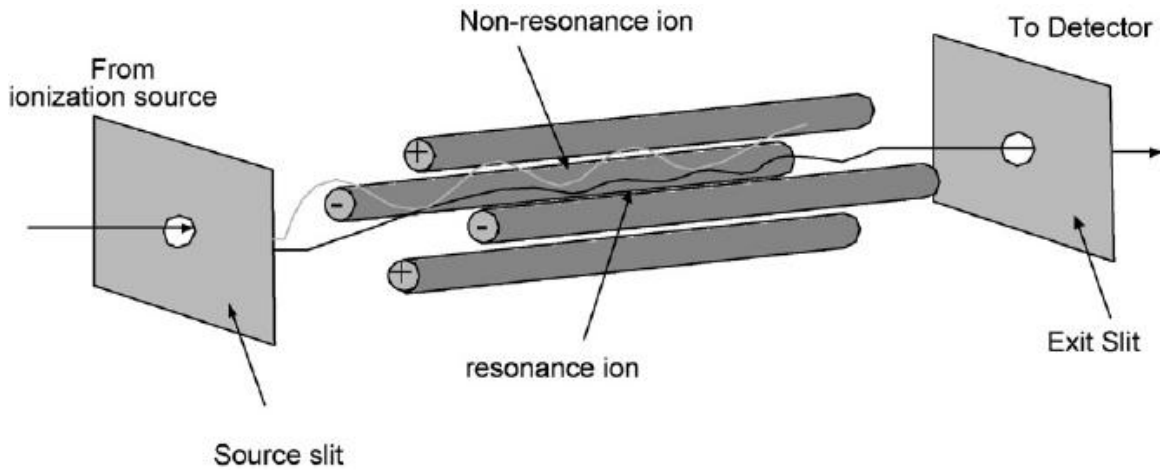

Figure 2.4: The schematic presentation of Quadrupole Mass Filter (QMF) *"https://www.researchgate.net/figure/6699273_fig6_Fig-8-A-schematic-of-a quadrupole mass-filter-Resonant-ions-will-travel-down-through"*

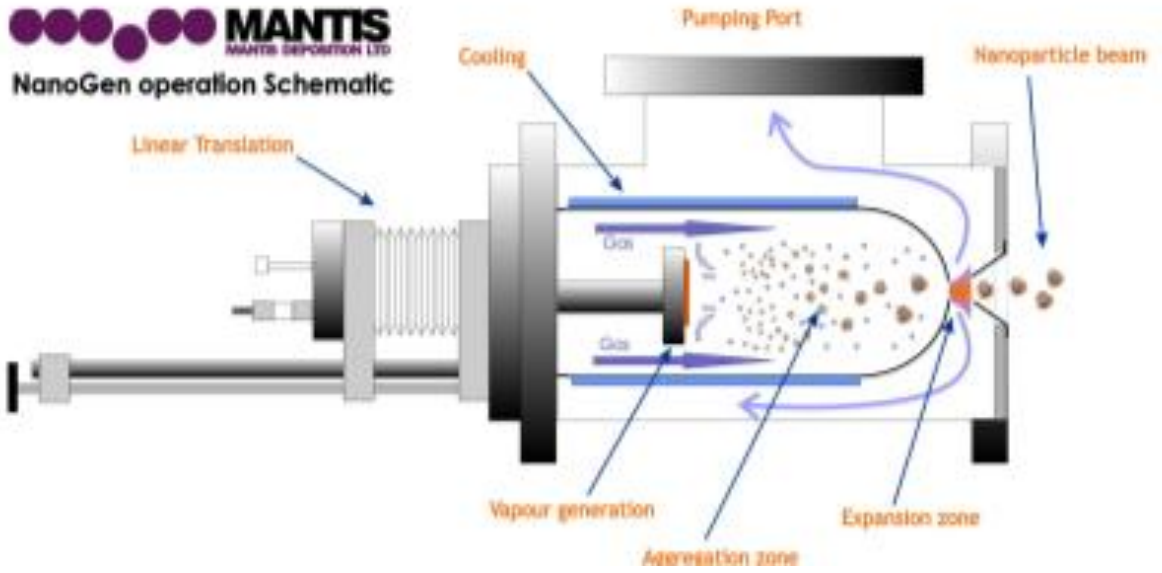

Figure 2.5: NanoGen operation schematic in the Mantis deposition system *(http://www.mantisdeposition.com/nanoparticlegenerators.html)*

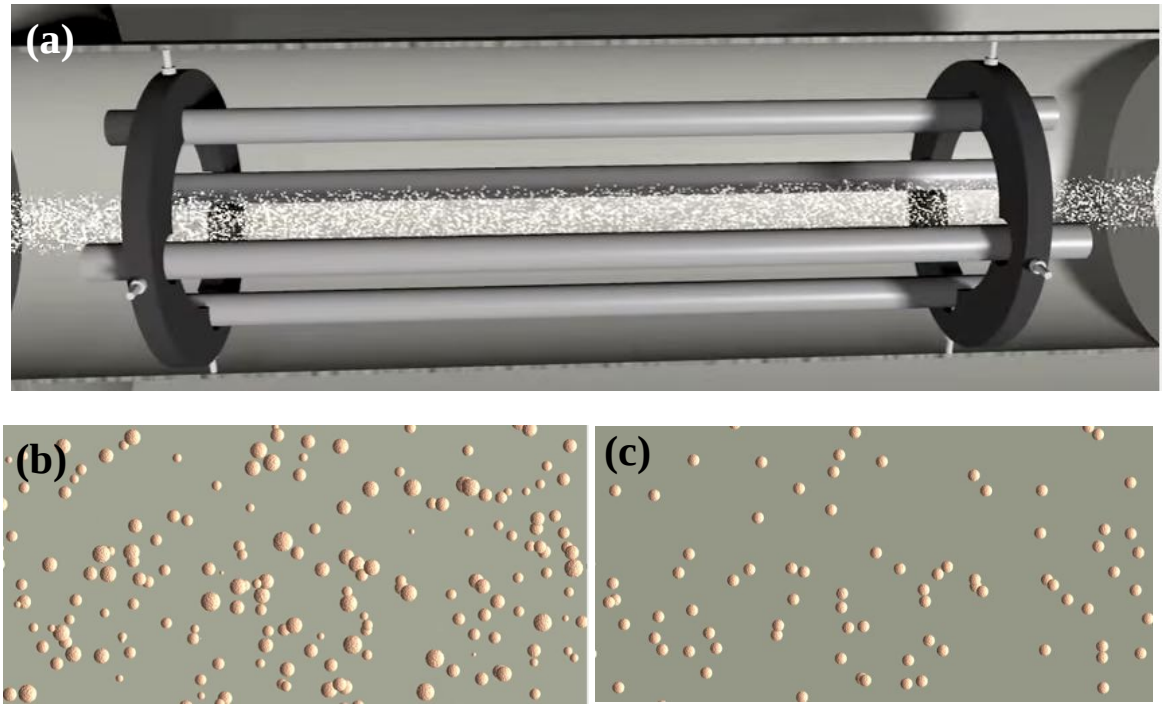

Figure 2.6: (a) Schematic presentation of the size filtration process in the QMF, (b) Nanoparticles before filtration, (c) Size-selected nanoparticles after filtration *(htt://wpww.youtube.com/watch?v=RNJKfIj8WlQ)*

2.2 Microbial Fuel Cell Construction and Operation

20 ml dual chamber MFCs were constructed and organized in arrays, each containing three cells. The MFC was assembled at Okinawa Institute of Science and Technology (OIST) Graduate University according to the manufacturer manual (MPowerWorld LLC, Russian Federation). Figure 2.7 includes two photographs showing the parts of the designed MFC.

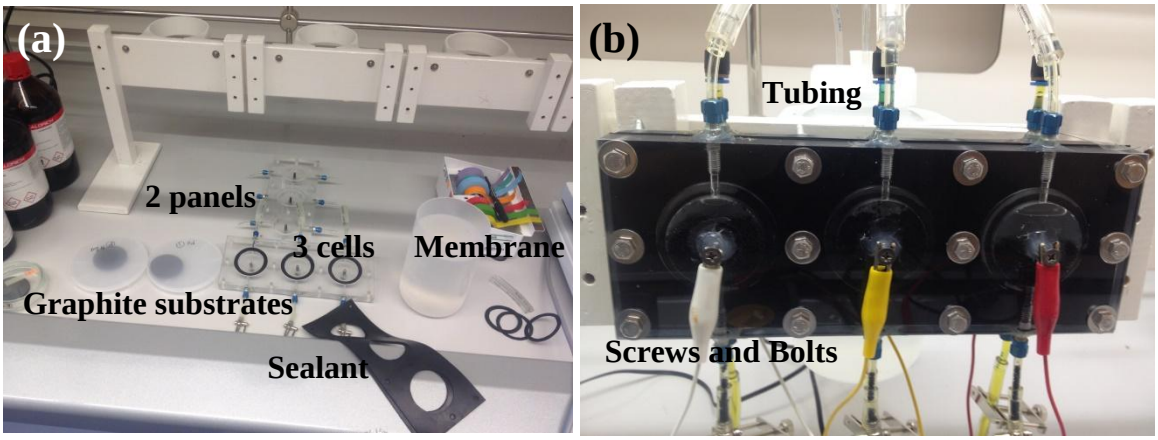

Figure 2.7: Main parts of the dual chamber microbial fuel cell; (a) MFC before assembly, (b) MFC after assembly ready to run *"Acquired at Okinawa Institute of Science and Technology"*

2.2.1 MFC Assembly (Experimental procedure)

- Materials were sterilized before using in the cell: panels were submerged in the sodium oxide and rinsed with distilled water, screws were treated for 1 hour with 70% ethanol and graphite substrates were immersed into isopropanol, sonicated and baked at 180 °C for 24 hours to evaporate isopropanol.

- Pd nanoparticle, MgO-Pd nanoparticle decorated and control graphite electrodes were inserted into the MFC's first panel and covered with a membrane. They all served as cell cathodes.
- The left three control graphite plates (anodes) were layered just above the previous set onto the separating membrane. Then the grooves of the second panel covered the panel down.
- Cell connections were performed by proper bolting and screwing.

- The cell was sealed to prevent leakage by applying a neutral sealant on the joint of the panels.
- The cell was left to dry for two days.

Figure 2.8: (a) sonication of graphite substrates, (b) MFC before assembly, (c) MFC after assembly *"Acquired at Okinawa Institute of Science and Technology"*

2.2.2 MFC Operation

- The internal volume of the cathode area was filled with 20 ml catholyte or electrolyte (potassium ferricyanide). The pH was adjusted to be 8 using 0.5 M NaOH solutions (tubes made of silicon were used to connect capillaries in and out).
- A proper amount of sludge (source of bacteria) was weighed (about 8.5 g) and filled in the internal volume of the anode area. The sludge was taken from an active MFC that has been operating for 8 months at awamori distillery site in Naha, Okinawa.
- The bacteria in the anode chamber was fed with acetate (organic substrate) to provide the bacteria with enough chemical energy throughout the experiment.

- MFC Voltage between the operating electrodes was recorded automatically and continuously by the digital data logger (Graphtec GL 820), where current was manually collected by the multimeter (TY530) three times a day.

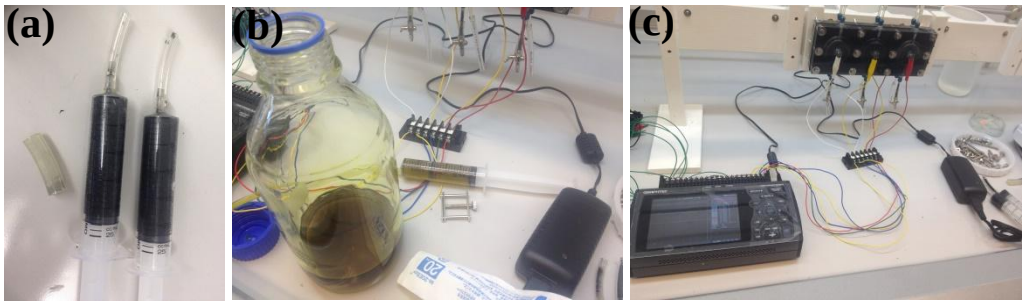

Figure 2.9: (a) Sludge includng bacteria, (b) Pottasium Ferricynide (electrolyte), (c) The running MFC *"Acquired at Okinawa Institute of Science and Technology"*

2.2.3 Materials and Equipment

2.2.3.1 Graphite electrodes

In all experiments involved in this study, graphite disks (49.5 mm × 3 mm) were used as the substrates for the growth of NPs and as the control as well in each test run.

Generally, carbon-based materials such as graphite, carbon paper and carbon cloth have good biocompatibility, good chemical stability, high conductivity and relatively low cost. Therefore, they have been extensively used for MFC anodes. However, the extent to which MFC's performance is improved depends highly on the electrode's configuration, which can have a plane, packed or brush structure. (Wei et al., 2011)

Graphite, shown in Figure 2.10, is a known form of carbon, which is composed of layers of hexagonal arrangements of carbon atoms, which are called graphene layers. The density of hexagonal graphite is ~ 2.25 g/cm^3. The distance between the layers is 0.335 nm and the distance between two bonded carbon atoms is 0.142 nm. Within the graphitic

layers, the bonding is trigonal sp^2 –hybrid σ –bonds with delocalized π-bonds within the layers. The interlayer spacing of 0.335 nm being larger than the C—C bond length of 0.142 nm, indicates no chemical bonding between the layers except the van der Waals forces of attraction (Cho et al., 2007). This structure gives the graphite its properties such as its high strength upon heating and low thermal expansion coefficient (thermal stability), good thermal and electrical conductivity and adequate machinability, which make graphite an ideal choice in MFC's anode side.

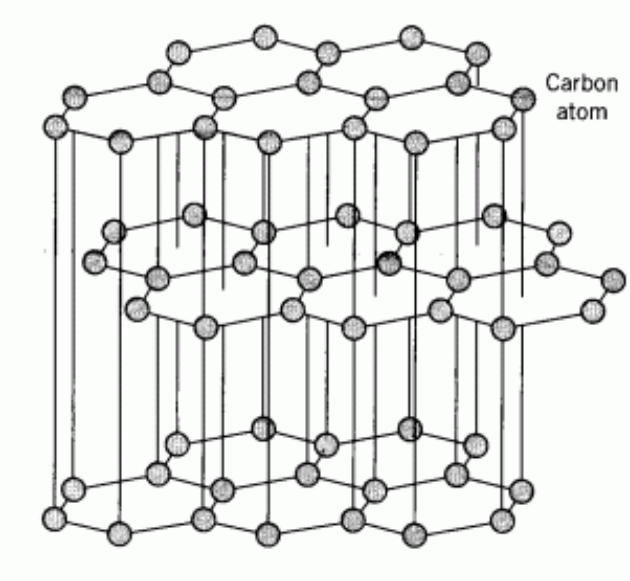

Figure 2.10: The structure of graphite in which carbon atoms are held together by strong covalent bonding in a hexagonal lattice structure forming expansive sheets loosely coupled together by much weaker van der Waals bonding between the layers. *(http://batteryblog.ca/2010/06/lithium-ion-anode-materials-ordered-and-disordered-carbon/)*

2.2.3.2 Electrolyte

Potassium ferricyanide (FeCN) was selected to serve as the electron mediator or electrolyte in the MFC used in this study because of its reported potential to increase the

power generation efficiency of the MFCs, especially when added to carbon/graphite electrodes, by improving the electron transfer from the bacterial cell to an electrode with a performance comparable to platinum (Lin et al., 2014).

Ferricyanide or hexacyanoferrate $Fe(CN)_6^{-3}$, which has a standard potential of 0.361V, is highly soluble in water. Using Ferricyanide in MFCs can cause a great improvement in power generation especially when compared with oxygen. This can be attributed to the fact that there's little polarization of the cathode; so that the achieved cathode potential is quite close to that calculated for standard conditions(Logan, 2010).

Thus, potassium ferricyanide was widely used as electron acceptor in studies of the two-chambered MFC (Wei et al., 2012). It's important to choose an appropriate concentration to improve MFC power generation because, according to Nernst equation and the kinetics of redox reaction, any changes in the electron accepter concentration can affect the MFC performance.

Electrolyte was analyzed using the cyclic voltammetry (CV), which is used to study the electrochemical properties of analyte in solution. In this research, the experiment was done using three-electrodes system; graphite electrode as the working electrode, platinum as the counter electrode and Ag/AgCl as the reference electrode. In the CV test, Figure 2.11, potential is applied between the working electrode and the reference electrode and current developed between the working and the counter electrodes is measured. The resulted current versus potential plot is analyzed to obtain information about redox potentials and electrochemical reaction rates, which gives an indication about the stability of the electrolyte and the reaction products.

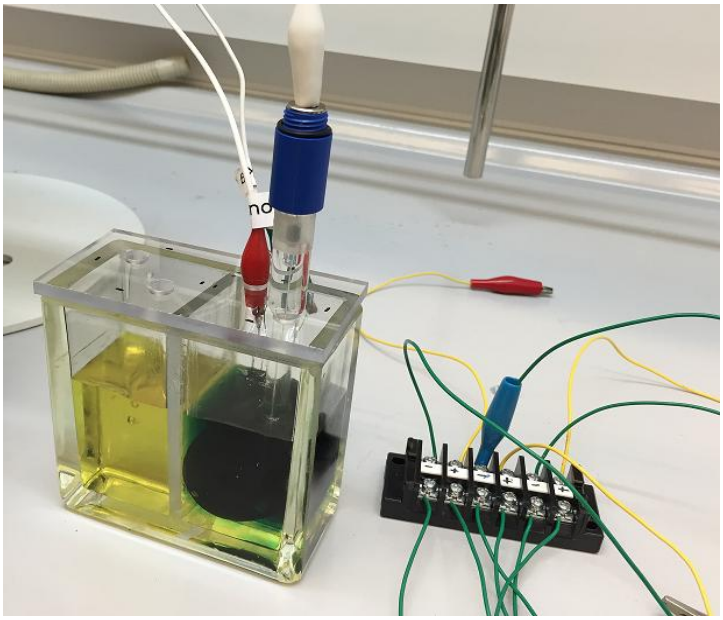

Figure 2.11: The cyclic voltammetry test performed on potassium ferricyanide *"Acquired at the Nanoparticle by Design Unit (Sowwan Unit) at Okinawa Institute of Science and Technology"*

2.2.3.3 Proton Exchange Membrane

For this work, Nafion-117 (175 microns 875X 225 mm) was used as a proton exchange membrane (PEM) in the designed MFC because of its known excellent affinity for protons.

Nafion, as illustrated in Figure 2.12, is an uncross-linked sulfonated tetrafluoroethylene copolymer, that is composed of a hydrophobic fluorocarbon backbone to which hydrophilic sulfonate groups are attached. In fact, the presence of the considerable amount of negatively charged sulfonate (HSO_3^-) groups in its structure results in the required high proton conductivity of Nafion making it a good choice as a PEM in MFCs despite of its undesirable affinity for other cations too (Chae et al., 2008). Besides,

Nafion membranes show good mechanical and chemical stability at high temperatures (Stenina et al., 2004).

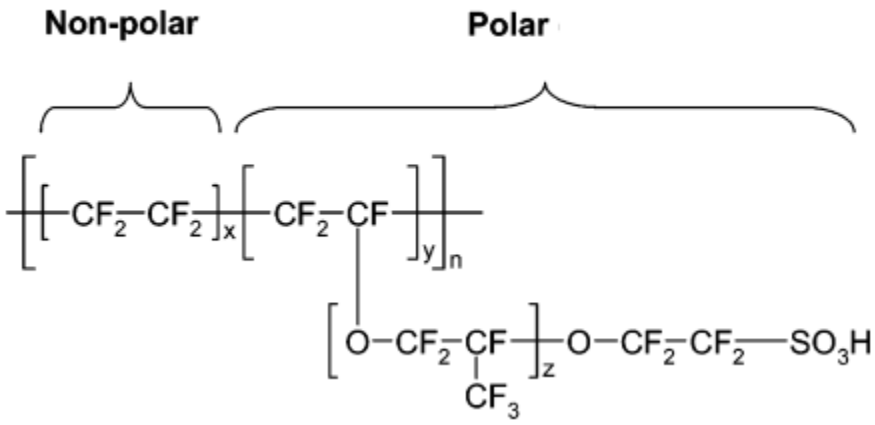

Figure 2.12: Chemical structure of Nafion. Nafion-117 has an average composition of x= 6.5, y= 1 and z= 1 *(Jang et al., 2004)*

PEMs are one of the most important components in MFCs, since they physically separate the anode and cathode compartments to prevent direct contact that leads to short circuiting. Most importantly, PEMs help in sustaining the electricity generated in the MFCs, by permitting protons transport through the electrolyte from the anodic side to the cathode, where they combine with the electrons and oxygen aided by catalyst, to form water (Chae et al., 2008). However, membranes can lead to pH gradients between the electrode chambers, and they can deform resulting in deterioration in the MFC's performance especially when the membrane is placed next to the cathode. In addition, the presence of a separating membrane between the MFC's chambers also increases the internal resistance by boosting the ohmic resistance of the cell due to reduced proton transport to the cathode, which means the power output of the MFC will decrease; as it's known that the distance across which proton transfer occurs from a membrane to a

cathode is positively correlated to the ohmic resistance of that cathode (Wei et al., 2011). Thus, MFC technology requires a system including some type of separator between electrodes with closest electrode spacing and improvement in power densities on a volumetric basis. This actually can be achieved if oxygen penetration to the anode can be reduced and proton transport is still facilitated. (Logan, 2010)

2.2.3.4 Buffer

Buffer was used to maintain a pH of 7 to ensure that the environment is suitable for bacterial growth. In addition, buffering of pH change and removal of the produced protons are very important for maintaining the potential of the anode, which will aid the generation of the greatest voltage.

2.2.3.5 Microorganisms and Medium

Sludge samples including bacteria were obtained from an active MFC, which has been operating for 8 months at awamori distillery site in Naha, Okinawa.

MFCs are BES that couple the oxidation of a substrate at a low redox potential with the reduction of an electron accepter at a higher redox potential, thus producing electricity. Microorganisms are used to catalyze one or both reactions at the electrode surface (Virdis et al., 2010)

2.2.3.6 Microbial substrate

Acetate ,in the form of sodium acetate CH_3COONa and concentration of 2 g/L, with different COD values was used as organic electron donor to feed the bacteria. It can be

easily digested and metabolized by microorganism that use the energy stored in this organic substrate and convert it into electrical energy.

2.3 Characterization Techniques

2.3.1 Scanning electron microscopy (SEM)

As an electron microscope, the SEM uses a high-energy beam of electrons to scan the surface of the sample giving information about the surface topography and chemical composition. The SEM main parts are the electron gun as a source of electrons, the column or the tube down which electrons propagate until they reach the sample and it also includes the electromagnetic lenses (condenser lenses and objective lenses), the sample chamber, the sample stage on which the sample is mounted and finally the computer and monitor as a display system.

The electrons are produced from a filament, usually a tungsten filament, accelerated down through a set of lenses that condense and focus the electron beam to finally form a fine probe of electrons, which hits the surface of the object. This beam scans the surface in a raster motion, which enables information about a defined area on the sample to be collected. As a result of the electron-sample interaction, high-energy electrons backscattered from the primary beam, secondary electron, with energies of a few tens of eV (Prior et al., 1999), and characteristic X-rays are generated. Eventually, these electrons are collected and detected by an appropriate detecting system to form an image ready to be analyzed.

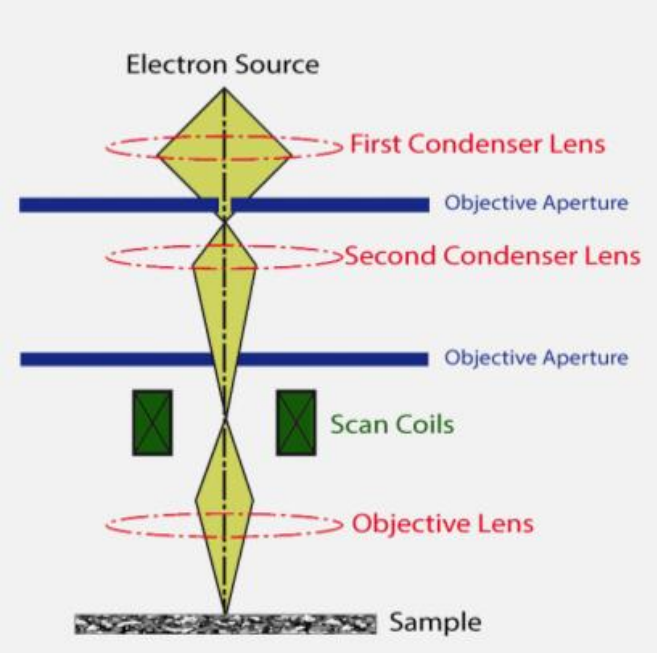

Figure 2.13: The main parts of the scanning electron microscope *(http://www.nanoscience.com/products/sem/technology-overview/how-sem-works/)*

In this study, surface morphology for plain and decorated electrodes was examined using SEM (SEM, FEI Quanta) utilizing the BSE (Z-contrast) and SE (topography contrast) imaging.

2.3.2 Atomic Force Microscopy (AFM)

Principle

Atomic force microscopy, which was invented by Gerd Binning et al. in 1986, is a type of scanning probe microscopy (SPM) with very high resolution (order fraction of a nanometer). With this microscopy, the surface of the sample is analyzed by being scanned using a probing tip that's attached to a cantilever, which is deflected in response to the force between the sample and the tip. (Binning et al., 1986; Meyer, 1992)

AFM is a novel characterization method for high resolution imaging of any surface including conductors, insulators, semiconductors, metals and oxides, biological molecules, polymers, clusters, nanoparticles and others. Using this powerful technique, surface topography, mechanical, electrical and magnetic characteristics can be studied both qualitatively and quantitatively. (Koznetsova et al., 2007)

AFM principle of operation is based on detecting the forces of interaction (repulsive and/or attractive surface forces) between the atoms of the sample and those of the tip that scans its surface while it's located close to it. Image contrast is generated by monitoring these forces. The tip is fabricated under a flexible cantilever responsible for the signal transduction. The cantilever bends or twists in a manner proportional to the interaction force. These bending and twisting actions are detected by a laser that's focused on the cantilever. The laser beam reflection is focused on the photodiode detector. The variation in the reflected beam's point of incidence in the photodiode is used to measure the interaction between the sample and the tip. This deflection is monitored during scanning and is translated into a 3D image of the surface. (Koznetsova et al., 2007)

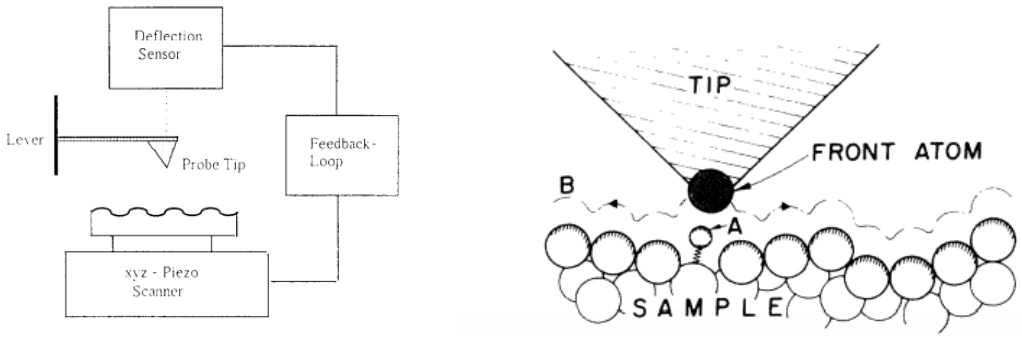

Figure 2.14: Basic principle of scanning samples using a sharp probing tip mounted on a cantilever-type spring in the AFM. The tip follows contour B to maintain constant force between tip and sample during scanning. *(Binning et al., 1986)*

Operating modes

AFM can be operated in a number of different probing or imaging or scanning modes depending on the nature of the interaction between the tip and the sample surface. The three main operating modes are the contact, non-contact and tapping modes.

Contact AFM: by using the contact mode, one can measure surface topography by sliding the probe tip across and in direct physical contact with the sample. The applied force on the sample is constant. The interatomic force between the tip and the sample is repulsive. As the tip scans the sample, cantilever is deflected and this deflection is measured by laser beam shift and feed back to the scanner. The distance is kept constant as the scanner readjusts its height.

Non-contact AFM: measures topography by sensing Van der Waals attractive forces between the sample's surface and the probe's tip held above the surface at a constant height. Images obtained by this mode have lower resolution than those obtained by using either contact mode or tapping mode.

Tapping mode: measures topography by tapping the sample's surface with an oscillating tip with low forces. This mode eliminates shear forces which can damage soft samples and reduce image resolution. Samples for this work were all characterized using the MM-SPM in tapping mode.

Tapping mode principle of operation:

A piezo stack excites the cantilever substrate vertically, causing the cantilever to move up and down and the reflected laser beam to deflect in a regular pattern over a photodiode array, generating a sinusoidal electronic signal. This signal is converted to a root mean square (RMS) amplitude value, which is displayed in volts on the upper left (tapping

output signal) meter located in the front of the multimode base. Although the piezo stack continues to excite the cantilever substrate with the same energy, the tip is deflected in its encounter with the surface. The reflected laser beam reveals information about the vertical height of the sample surface and characteristics of the sample material itself, such as elasticity, magnetism and presence of electrical forces. *(MM-SPM manual at OIST)*

Other methods or modes are also available in the multimode scanning probe microscopy (MM-SPM), which are:

Phase imaging: provides image contrast cause by differences in surface adhesion and viscoelasticity.

Lift mode: combines tapping mode to study surface topography with another selected property such as magnetic or electric force.

Magnetic force microscopy (MFM): for measuring some magnetic properties of the analyzed sample.

Lateral force microscopy (LFM): measures frictional forces between the tip and the sample's surface.

Scanning tunneling microscopy (STM): measures surface topography of conductive samples using a tunneling current.

Electrochemical microscopy (ECSTM and ECAFM): measures topography and some properties of conductive materials that are immersed in electrolyte solutions with or without potential control.

Lithography: for micro-hardness testing by indenting the sample's surface, or to generate patterns by scribing.

Torsional resonance mode (Tr mode): studies surface properties by oscillating the cantilever in torsion.

For this study, AFM measurements were conducted in a glovebox atmosphere (<0.1ppm O_2 and <1ppm water) using a Multimode 8 (Bruker, Santa Barbara, CA). The AFM system is equipped with the NanoScope-V controller in tapping mode using triangular silicon-nitride AFM tip (radius <10 nm, force constant of 9 Nm^{-1}, 150 kHZ of resonant frequency, OLYMPUS). The AFM system height ‘‘Z’’ resolution and noise floor are less than 0.030 nm. The scanning probe processor (SPIP) (Image Metrology, Hørsholm, DK) software was employed for the AFM image analysis.

2.3.3 Transmission Electron Microscopy (TEM)

Transmission electron microscope (TEM) is a powerful and unique technique for studying and investigating material’s structure. Characterization occurs when a high energy beam of electrons (electron probe) is transmitted through the very thin sample being analyzed, as the interactions between these electrons and the atoms of the sample can reveal some important structural features such as crystal structure, dislocations and grain boundaries. The most important feature in the TEM is the atomic-resolution real-space imaging of NPs. Furthermore, due to the nanometer size electron probe in the TEM, it can be used to identify and quantify the chemical and electronic structure of individual nanocrystals.

Although scanning tunneling microscopy and atomic force microscopy can provide atomic-resolution images of large crystal surfaces, they are unlikely to clearly resolve the atomic lattices of nanoparticles because of the surface coating and the wobbling of the

nanocrystals under the scanning tip. On the other hand, TEM can powerfully reveal the atoms distributions on nanocrystal surfaces even when they are passivated with polymers. (Wang, 2000).

High-resolution TEM components

The HRTEM is mainly composed of an illumination system, a specimen stage, the objective lenses, the magnification system, the data recording system and the chemical analysis system. The illumination system includes the electron gun and the condenser lenses. The specimen stage has a distinctive feature in performing the structural analysis, because it can help in characterizing the physical properties of individual nanostructures, as it's the main part being used in the in-situ observations of phenomena induced by annealing, electric field, or mechanical stress. The objective lens system is vitally important as it mainly determines the resolution of the TEM image. The intermediate and projection lenses are included in the magnification system, which gives a magnification up to 1.5 million. The data recording system allows quantitative data processing and quantification. Finally, the chemical analysis system is the energy-dispersive X-ray spectroscopy (EDS) and electron energy loss spectroscopy (EELS), both can be used complementary to quantify the chemical composition of the specimen.

TEM principle of working

The electron gun in the TEM includes a filament that's heated up with an amount of heat large enough to cause the filament to release and accelerate electrons. These electrons should have very short wavelengths and high enough speed to illuminate the sample and pass through it effectively. Then the released electrons continue their path as a beam into

the vacuum tube that contains the TEM lenses. All these lenses are magnetic, serving as anode, which helps the negative electrons to propagate along the vacuum, as these lenses are positively charged and available as large number of magnetic coils, which are responsible to the generation of a very high magnetic field leading electron beam to be precisely directed to the specimen in a very fast speed as required. The electron beam is projected onto the ultrathin sample by means of the condenser lens system. This beams is finally transmitted through the ultrathin specimen and diffracted by the lattices of the crystal leading to gathering structural information. The propagation of the electrons through the objective lens is the main source of nonlinear information transfer in the TEM. The obtained signal isn't actually magnified enough to be presented, therefore other type of lenses (intermediate and projection lenses) are incorporated within the TEM structure to amplify that signal and eventually detected and projected onto the screen to be finally imaged.

TEM applications

In addition to the TEM's capability of internal structural characterization and chemical analysis, it has also other applications in nanotechnology. For example, it can be used to determine the melting points of nanocrystals, in which, an electron beam is used to heat up the nanocrystals and the melting points are recorded once the electron diffraction is disappeared. Moreover, the in situ TEM can be used to characterize and measure mechanical and electrical properties of individual nanostructures such as nanowires and

nanotubes. This technique allows the structure-property relationship to be clearly registered to a specific nanoparticle structure. (Wang, 2000)

For this research, TEM studies were carried out using an FEI Titan microscope in OIST, operated at 300 kV, equipped with a spherical aberration corrector for the TEM imaging. In TEM mode, the spherical and chromatic aberrations were <5 µm and 1.4 mm, respectively, with an optimum resolution of better than 0.09 nm.

Figure 2.15: The transmission electron microscope- FEI Titan *"Acquired at Okinawa Institute of Science and Technology"*

2.3.4 X-ray Photoelectron Spectroscopy (XPS)

X-ray Photoelectron Spectroscopy (XPS) is a quantitative surface-sensitive spectroscopic technique. It's a valuable and powerful method that's widely used in many fields of study for analyzing chemical composition and bonding states. (Yang et al., 2009)

Surface analysis in XPS is accomplished by irradiating the sample's topmost atomic layer (≤100 °A) in a high vacuum chamber with a monochromatic X-ray beam. The X-ray

beam causes electrons from the surface of the solid sample to escape. The number of the emitted electrons and their kinetic energy are simultaneously detected and measured. These characteristic electrons have a specific energy spectrum or energy distribution (a fingerprint) depending on the element and its chemical bonding state. This fingerprint contain information about chemical oxidation state, electronic structure and atomic composition of the sample being analyzed. Thus, using XPS is beneficial in determining the surface chemical composition as well as the electronic environment. (Chusuei et al., 2002)

The principle of operation of the XPS relies on the photoelectric effect, which occurs via a primary excitation process brought about by X-ray irradiation producing electrons called the photoelectrons. The photoelectrons with their discrete energy carry chemical information about the surface layer.

In the photoemission process, an atom absorbs a photon of a known energy ($h\nu$) resulting in the emission of a core level electron (photoelectron) which is detected and its kinetic energy (E_k) of the sample is measured. The Fermi level (E_F) is the common reference for measuring the electron energy in surface studies. Figure 2.16 illustrates the energy level condition in a metallic surface. The sample is electrically connected with the spectrometer so that their Fermi levels are the same. The kinetic energy of the photoelectron at the sample surface (E_k^1) relative to the vacuum level (E_v) is determined from the kinetic energy of the electron (E_k) measured inside the spectrometer by using the following equation:

$$E_k = E_k^1 - (\emptyset_{spec} - \emptyset_s) \qquad 2.1$$

Where $Ø_{spec}$ and $Ø_s$ are the work functions, or energies required to remove the electrons from the Fermi to the vacuum levels, of the spectrometer and sample, respectively.

The binding energy of the atomic orbital from which the electron originates (E_b), accordingly, can be obtained using this relation:

$$E_b = h\nu - E_k - Ø_{spec} \qquad 2.2$$

the binding energy can be regarded as the energy difference between the initial and the final states after the photoelectron has been emitted from the atom. However, there is a variety of kinetic energies of the ejected electrons, because of the different possible final states of the ions from each type of atom.

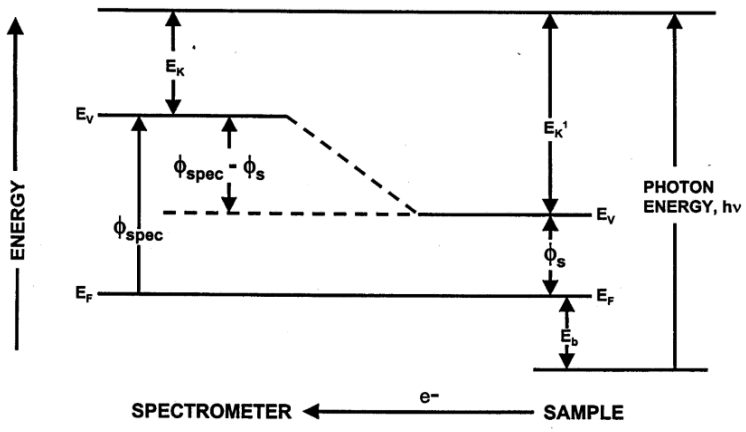

Figure 2.16: Schematic representation of energy level for the XPS process *(Chusuei et al., 2002)*

For this research, the XPS measurements were performed in a Kratos AXIS Ultra DLD Photoelectron Spectrometer, with an Al Kα (1486.6 eV) source and a base pressure of $10^{(-10)}$ mbar. The Mg 2p, Mg 2s, Pd 3d and C 1s core level narrow spectra were recorded using pass energy of 20 eV for high resolution. The XPS photograph is shown in Figure 2.17.

Figure 2.17: The X-ray Photoelectron Spectroscope *"Acquired at Okinawa Institute of Science and Technology"*

2.3.5 X-ray Diffraction (XRD)

X-ray diffraction or X-ray crystallography is one of the most important and useful characterization tools used to reveal the crystallographic structure and chemical composition of solid state crystalline materials.

The constituents (atoms, molecules or ions) of a solid crystalline material can form a regular three dimensional arrangement or array of particles in space called crystal lattice or space lattice. Atoms within the crystal lattice are distributed so that they form successive parallel planes separated from one another by a spacing distance d, which is distinctive for each crystal structure depending on the nature of the material. So each crystal structure, when exposed to X-rays, forms a characteristic pattern that can be used as a fingerprint for identifying the material.

The characteristic diffraction pattern can only be produced if the Bragg's law conditions are satisfied; that is Bragg diffraction will only occur if a monochromatic X-ray beam of wavelength λ is incident on a crystalline solid at angle θ and the X-rays interfere constructively when reflected from successive planes after they traveled a total distance that differs by a whole number multiple of their wavelength; i.e., the waves are fully in-phase, which is expressed in the following equation known as Bragg's law:

$$n\lambda = 2d\sin(\theta) \qquad 2.3$$

Where n is an integer and d is the planar spacing or separating distance. If λ is known and θ can be measured, the separation distance between atoms can be found and this is the basis of the process known as XRD.

X-ray is produced by by exciting or bombarding a metal target (Cu, Mo usually) with a beam of electrons emitted from w hot filament usually tungsten. The incident beam will ionize electrons in the K-shell (1s) of the target atom and X-ray emitted as the resultant vacancies are filled with electrons coming down from the L (2p) or M (3p) levels. This gives rise to $K\alpha$ and $K\beta$ lines.

Since X-rays primarily interact with electrons in atoms, information about the electron distribution in materials can be obtained from the measured elastically scattered X-rays. Diffracted waves from different atoms can interfere with each other and the resultant intensity distribution is strongly dependent on this interaction. Sharp interference maxima or peaks will be resulted if the atoms are periodically arranged as in crystals, which have the same symmetry as atoms distribution manner. Plotting intensities versus angular positions of the resultant diffracted peaks generates the characteristic pattern.

Hence, applying XRD experiments can be the source of information about lattice parameters, phase identity, phase purity, crystallinity, crystal structure (determine how the atoms pack together in the crystalline state, the interatomic distance, bond angle and size and shape of the unit cell) and % phase composition. *(http://electrons.wikidot.com/x-ray-diffraction-and-bragg-s-law)*

Grazing incidence XRD (GI-XRD) was performed on the electrodes used in this research. It's actually used for observing X-ray diffraction from thin films. In this technique, the diffraction volume is increased by decreasing the incidence angle to avoid getting weak diffraction intensities. The used GI-XRD is shown in Figure 2.18.

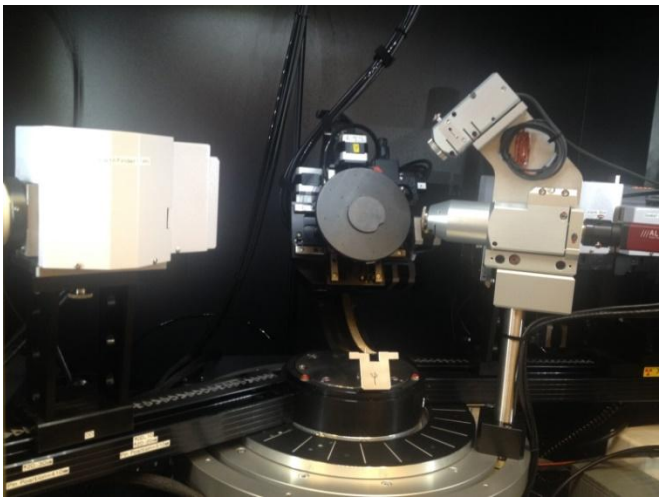

Figure 2.18: X-ray diffraction. GI-XRD applied on decorated graphite plates. *"Acquired at Okinawa Institute of Science and Technoloy*

Chapter Three

Results and Discussion

Simple Pd and MgO-Pd core shell nanoparticles were characterized using several techniques including the scanning electron microscopy (SEM) to reveal morphology and shape of NPs, Atomic Force Microscopy (AFM) to show topography of the NPs decorated electrodes and to evaluate NPs height, Transmission Electron Microscopy (TEM) for determination of NPs size distribution and crystal structure, X-ray Photoelectron Spectroscopy (XPS) to investigate the elemental composition of the surfaces of the NPs decorated electrodes, Grazing Incidence X-ray Diffraction (GI-XRD) to obtain structural and crystallographic information about the samples.

3.1 Imaging of Prepared Nanoparticles- SEM Characterization

SEM characterization was performed to study morphology and analyze the surface of the plain and NPs-decorated graphite substrates.

SEM images for plain graphite electrodes shown in Figure 3.1 reveals the morphology of the surface. In these images, carbon flakes and high surface roughness can be noticed. This surface roughness and associated high porosity result in larger surface area, which is beneficial for the attachment and adhesion bonding of microbes on the anodic side and for promoting the redox reaction in the cathodic side as well. In Fact, this can justify the selection of graphite substrates as electrodes in MFCs beside its reasonable price and other attractive required properties.

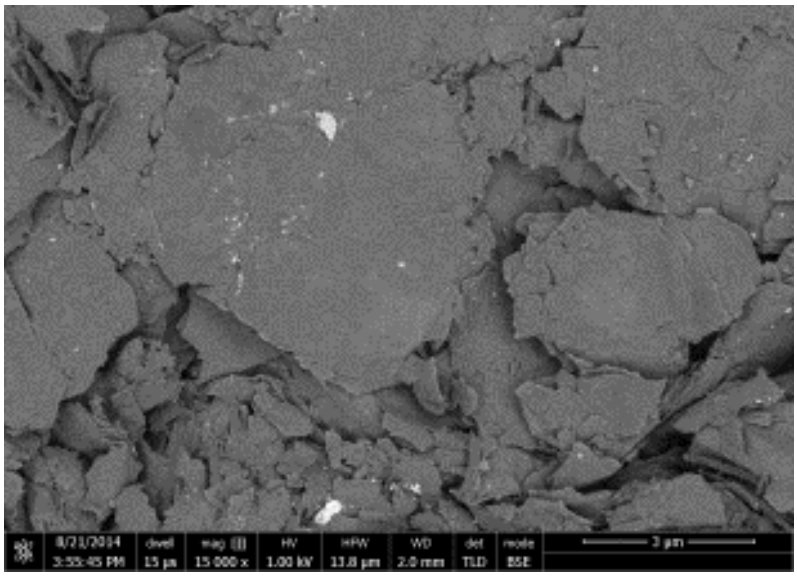

Figure 3.1: SEM image of plain graphite electrode, showing the very rough and porous surface of graphite. *"Acquired at Okinawa Institute of Science and Technology"*

As shown in Figure 3.2, it's obviously apparent that depositions with the ultra-fine particles have changed the substrate surface and that the electrodes became more porous. The surface is highly covered with the NPs due to the relatively long deposition time; 80 and 60 minutes for Pd and MgO-Pd NPs, respectively). It can also be noticed that the formed nanoparticle films might undergo some coalescence.

Actually, NPs coverage is very important because it can highly affect the extent to which power generation in MFCs can be enhanced. However, highly covered electrodes, especially when NPs coagulate or coalesce, may sometimes adversely affect the produced current due to the blocking sites at the electrode's surface. So, it's highly recommended to optimize NPs coverage.

More importantly to notice is that thin films of simple Pd NPs and MgO-Pd core-shell NPs have different nucleation and film growth behaviors, as revealed from the SEM

micrographs shown in Figure 3.2, which results in surfaces with different porosities, suggesting an interesting point to start with as a future work and study more to investigate the effect of film growth behavior on electrodes performance.

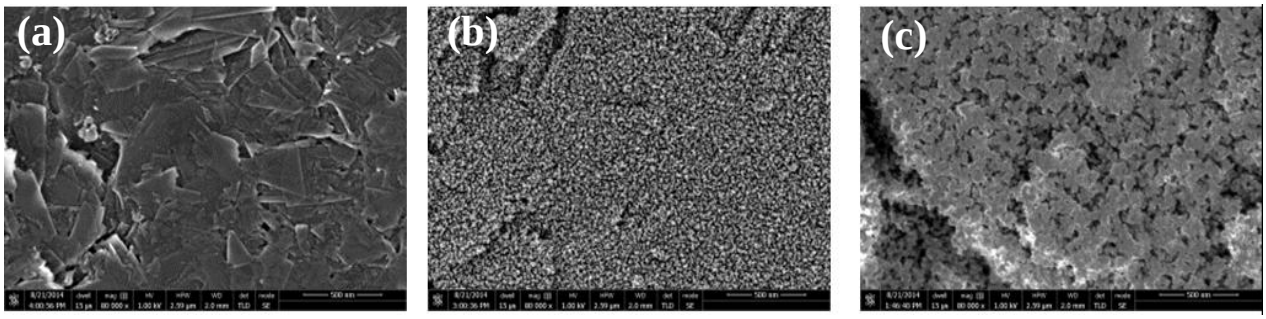

Figure 3.2: SEM images of MFC electrodes with and without nanodecoration. (a) Plain graphite electrode (control). (b) Pd NPs decorated graphite electrode. (c) MgO-Pd core-shell NPs decorated graphite electrode. *"Acquired at Okinawa Institute of Science and Technology"*

When thin films of MgO-Pd NPs were examined and imaged using a better magnification, the core-shell nanostructure of the NPs was clearly revealed as demonstrated in Figure 3.3; the white bright dots are expected to be the metallic Pd cores while the darker surrounding regions are the magnesium oxide shells. So the novel core-shell nanostructure with unique nucleation behavior was successfully synthesized using the DC magnetron sputtering technique.

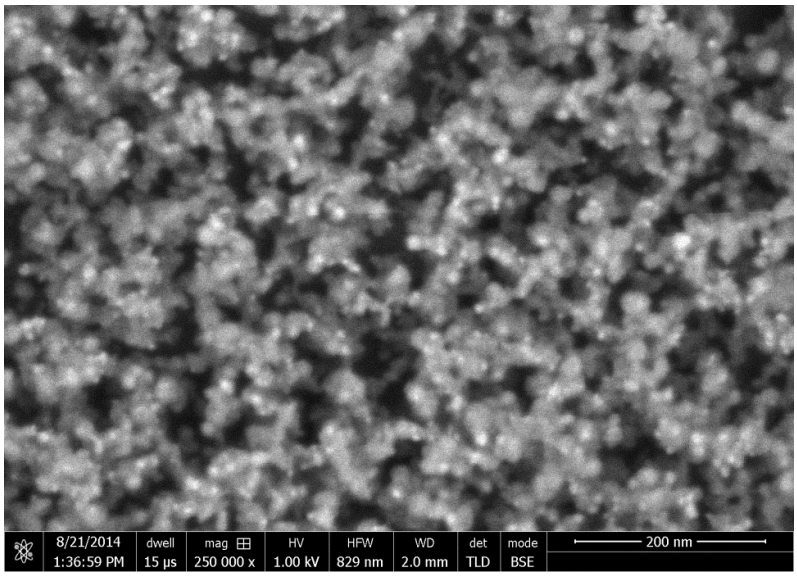

Figure 3.3: SEM image of Magnesium oxide encapsulated Palladium nanocatalysts deposited on graphite substrate; white dots represent the Pd cores while the darker regions are the magnesium oxide shells. *"Acquired at Okinawa Institute of Science and Technology"*

3.2 Topographical analysis- AFM Characterization

Prior to deposition, the size distribution of Pd NPs in the sputter generated beam was measured by the QMF. The Mantis deposition system is equipped with the QMF that is used to size select the NPs. Both distribution curves, demonstrated in Figure 3.4, are fitted quite well with a Gaussian curve with a peak at 2.5 nm and 5 nm. So it's clear that this deposition system results in the deposition of certain size distribution, which should be confirmed with the AFM analysis.

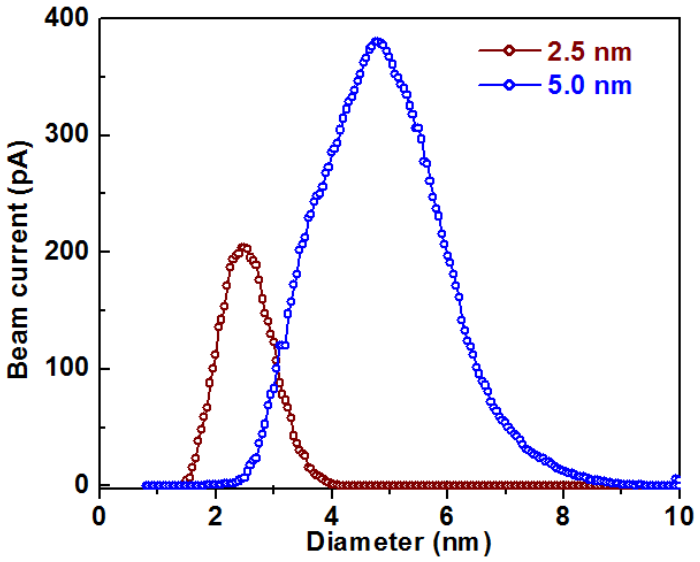

Figure 3.4: In-situ quadrupole mass filter (QMF) profile for two different Pd nanoparticles (2.5 nm and 5.0 nm average diameters). *"Acquired at Okinawa Institute of Science and Technology"*

The AFM images of deposited 2.5 nm Pd NPs, 5 nm Pd NPs and MgO-Pd NPs (9 nm), prepared by gas-aggregated sputtering are shown in Figure 3.5, Figure 3.6 and Figure 3.7, respectively.

The AFM topography data for the Pd NP film shown in Figure 3.5 indicates that the height of the Pd NPs is 2.4±0.3 nm, which is consistent with the QMF size selection (2.5 nm). As for the 5 nm size selected Pd NP film topography shown in Figure 3.6, the height is 4.9±0.7 nm, which is also consistent with the QMF size selection data. It can also be noticed for both depositions that the surface is highly covered and relatively rough as a result of the possible stacking or accumulation of multiple layers of NPs which confirmed the fact that Pd nanoparticles tend to agglomerate and coalesce with time.

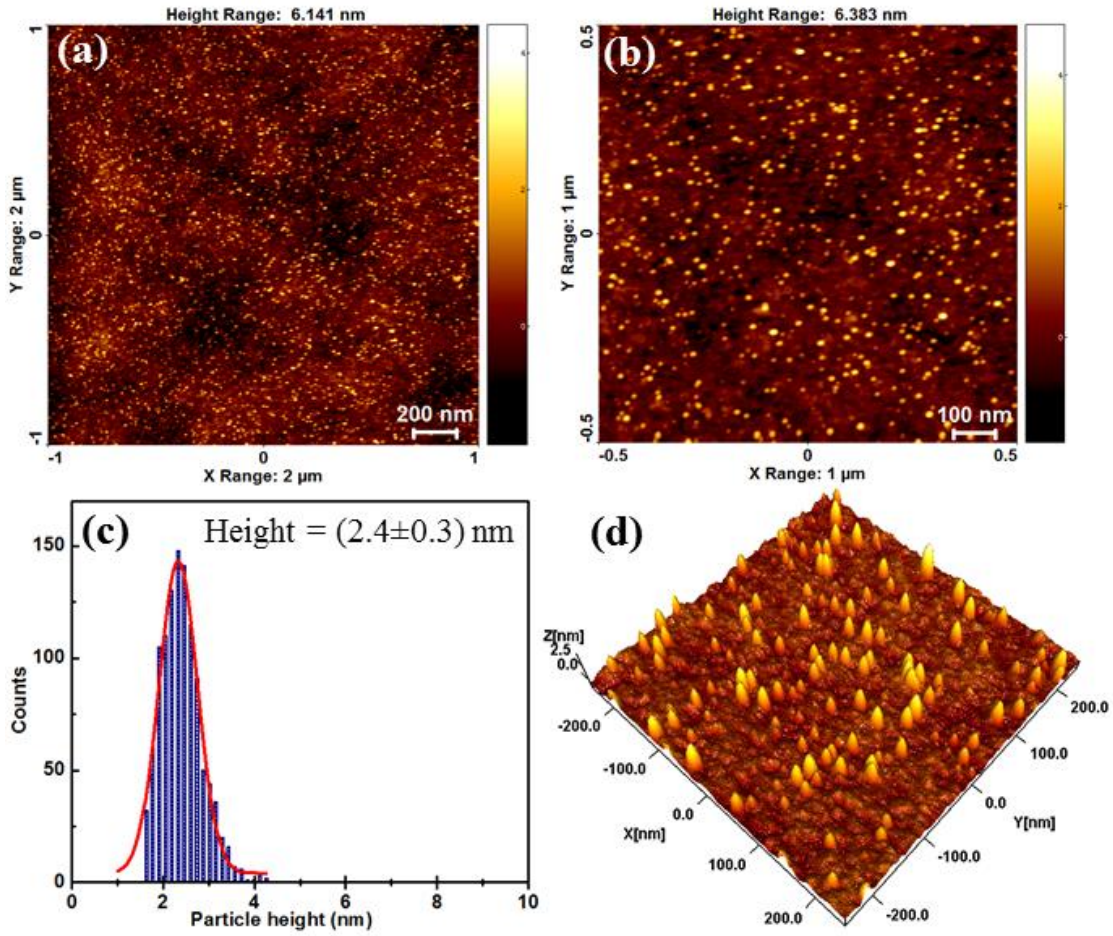

Figure 3.5: Atomic force microscopy topographical image from 2.5 nm QMF filtered Pd nanoparticles deposited on Silicon substrate. (a) Low magnification AFM image. (b) High magnification AFM image. (c) Particle height histogram obtained from the height of the nanoparticles and Gaussian fit (red line). (d) 3D AFM image from area 500 × 500 nm^2. Deposition conditions: Ar (50 sccm), He (10 sccm), Agg. Length (40 mm) and DC magnetron Power (6W). *"Acquired at Okinawa Institute of Science and Technology"*

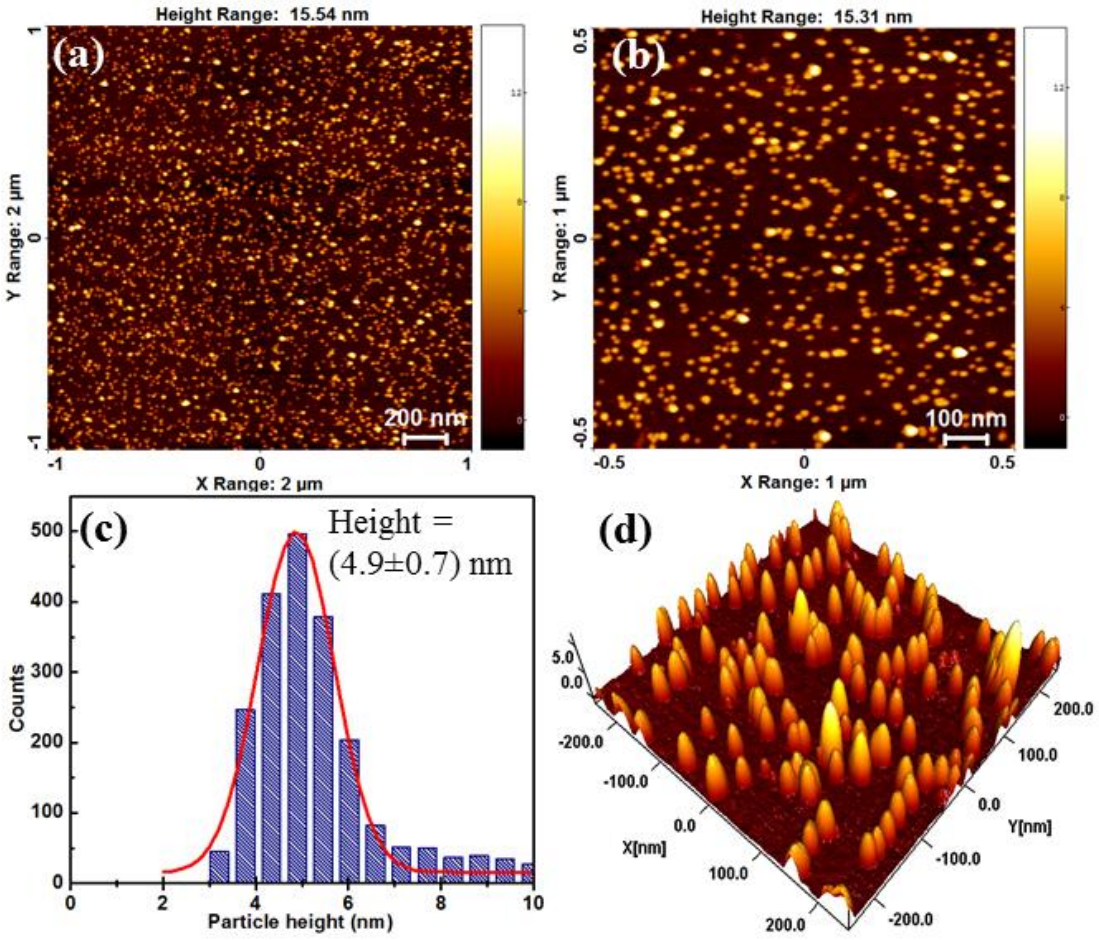

Figure 3.6: Atomic force microscopy topographical image from 5.0 nm QMF filtered Pd nanoparticles deposited on Silicon substrate. (a) Low magnification AFM image. (b) High magnification AFM image. (c) Particle height histogram obtained from the height of the nanoparticles and Gaussian fit (red line). (d) 3D AFM image from area 500 × 500 nm^2. Deposition conditions: Ar (70 sccm), He (0.0 sccm), Agg. Length (100 mm) and DC magnetron Power (15W). *"Acquired at Okinawa Institute of Science and Technology"*

Figure 3.7 shows the in-situ QMF profile for individual Mg, Pd and Mg-Pd nanoparticles.

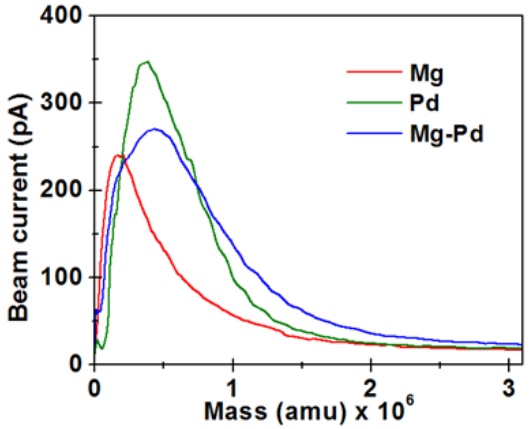

Figure 3.7 In-situ quadrupole mass filter (QMF) profile for individual Mg, Pd and MgO-Pd nanoparticles. *"Acquired at Okinawa Institute of Science and Technology"*

Figure 3.8 shows the AFM characterization and Z-height profile for the MgO encapsulated Pd NPs placed on silicon substrate. Figure 3.8 (a) shows the high density or coverage of the spherically shaped NPs, due to the deposition and accumulation of a large number MgO-Pd ultra-fine particles. The Z-height profile demonstrated in Figure 3.8 (b) indicates the NPs height is of about 9 nm.

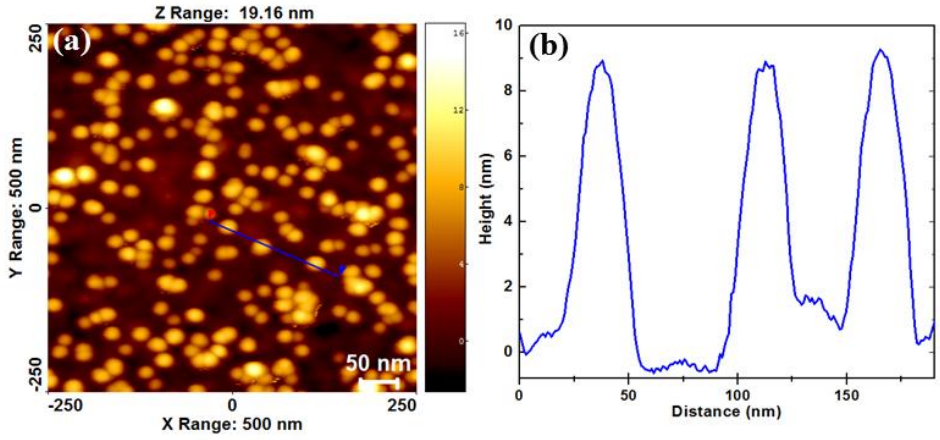

Figure 3.8: (a) AFM image and (b) Z-Height profile along the line indicated in (a), height (~9.0 nm) of MgO-Pd nanoparticles. *"Acquired at Okinawa Institute of Science and Technology"*

3.3 Particle Size Distribution and Crystallinity- TEM Characterization

TEM images for 2.5 nm and 5 nm Pd NPs are shown in Figure 3.9 and Figure 3.10, respectively.

Figure 3.9 shows (a) a low magnification TEM image, (b) the associated particle size histogram and(c, d) high resolution TEM images of Pd NPs synthesized by PVD-IGC technique (Mantis Deposition Ltd, UK). The spherical shaped Pd NPs can be clearly visualized. The particle size distribution histogram shows a distribution between 1.2 nm and 4.3 nm and the Gaussian fitting curve has an obvious peak at 2.7±0.3 nm, which is consistent with the particle size obtained using the AFM. The HRTEM images show that the Pd NPs are crystalline and has a defined crystal structure which is a cubic structure {111} with lattice parameter or atomic spacing (d) of 0.23 nm.

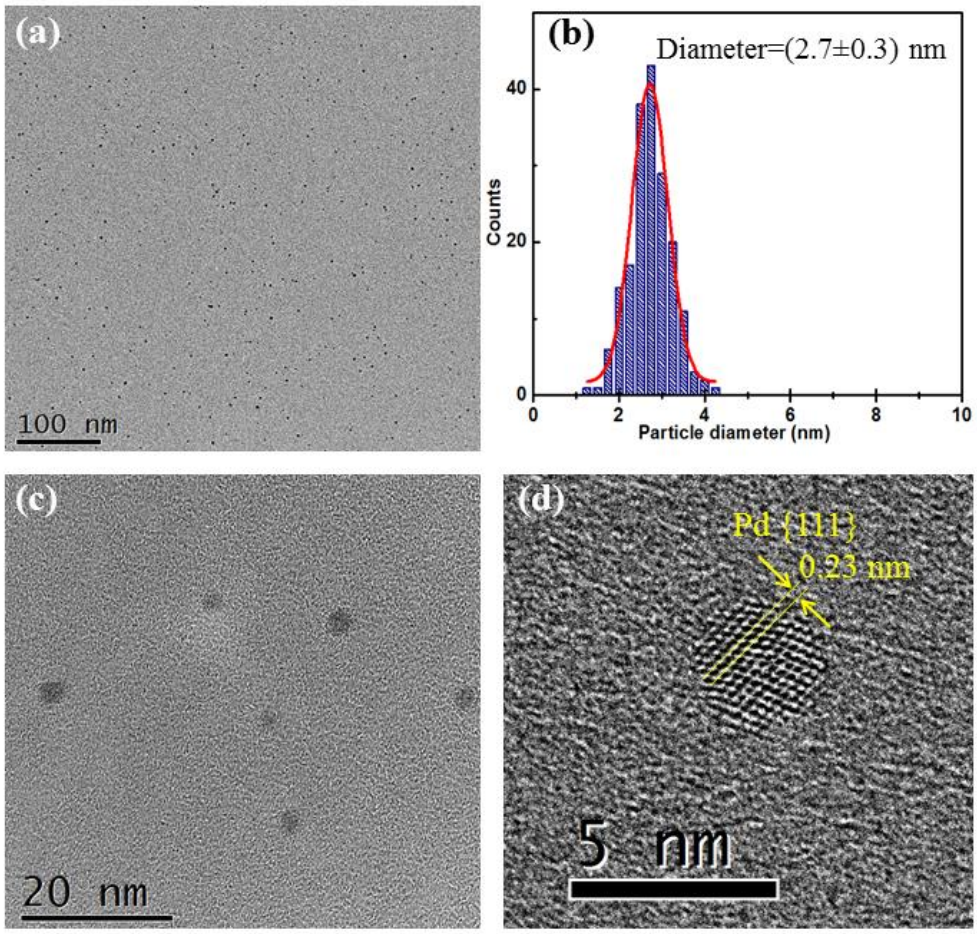

Figure 3.9: TEM images of (a) low magnification, (b) particle size distribution histogram and Gaussian fit (red line), and (c, d) HRTEM images of 2.5 nm Pd nanoparticles. *"Acquired at Okinawa Institute of Science and Technology"*

Figure 3.10 shows the TEM micrographs for 5 nm Pd NPs, particle shape is spherical and the Gaussian curve for particle size distribution shows a peak at 5.0±0.5, which suggests a particle diameter that's appropriate with that obtained by the AFM analysis. As for the crystalline structure of these NPs, it's apparent from Figure 3.10 (d) that the particles still have the same structure and lattice parameters as the 2.5 nm Pd NPs discussed in the previous paragraph. So it can be concluded that the Pd crystalline structure isn't actually

affected by changing the cluster size and it remains the same as long as same deposition technique and parameters are applied.

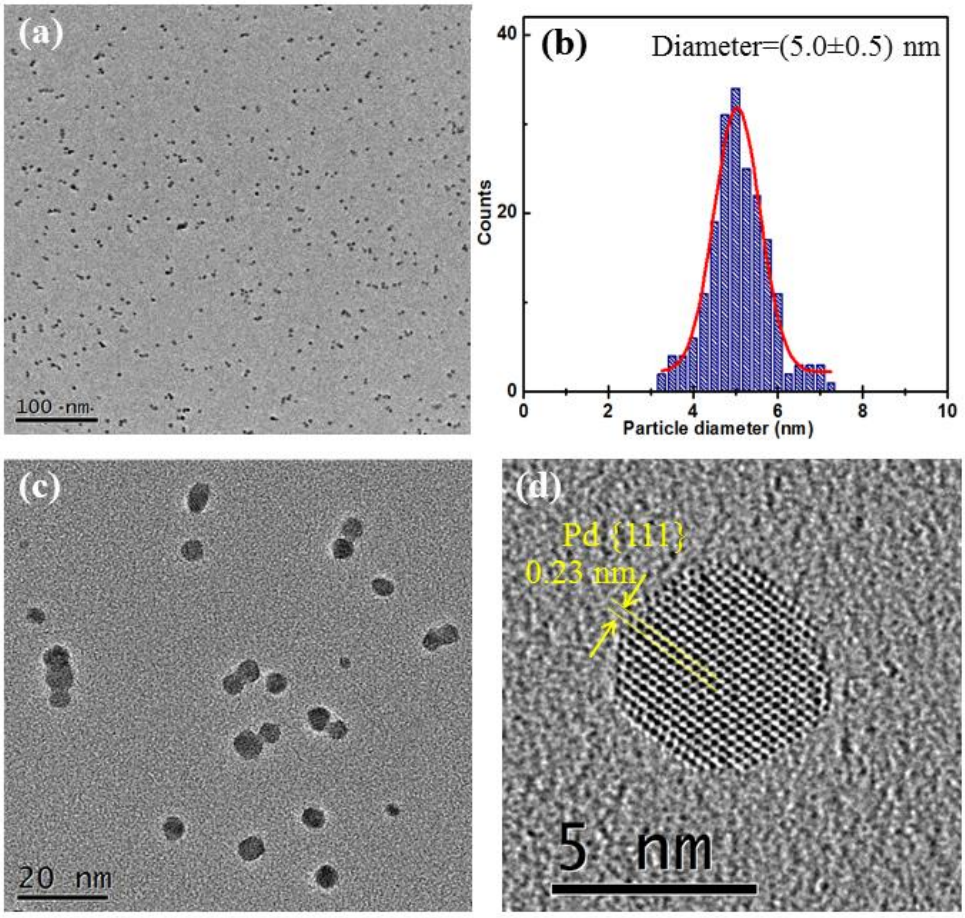

Figure 3.10: TEM images of (a) low magnification, (b) particle size distribution histogram and Gaussian fit (red line), and (c, d) HRTEM images of 5.0 nm Pd nanoparticles. *"Acquired at Okinawa Institute of Science and Technology"*

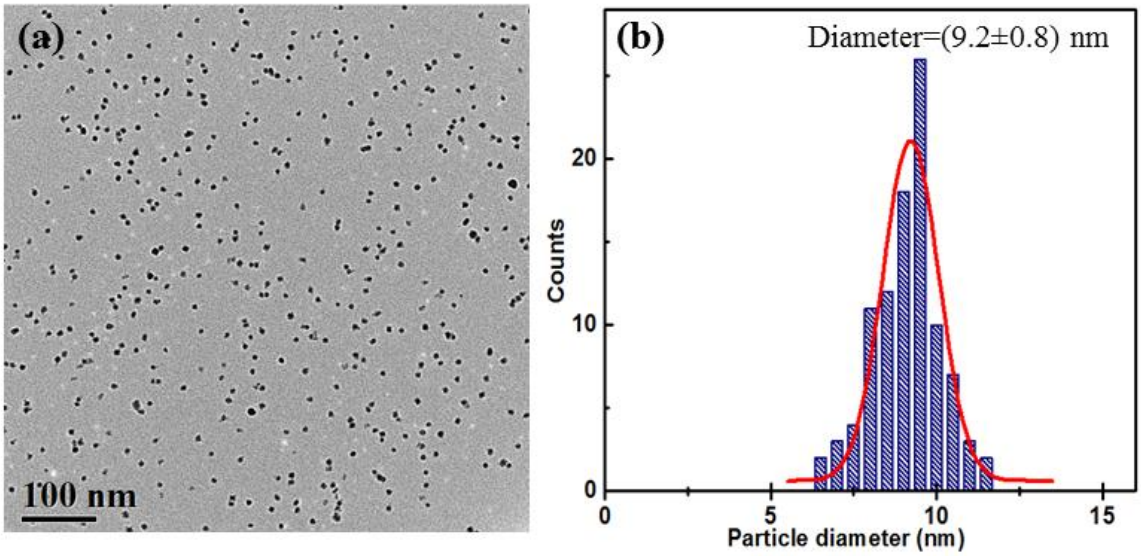

Figure 3.11: (a) TEM image and (b) particle size distribution histogram with Gaussian fit (red line) of 9.0 nm binary MgO-Pd nanoparticles. *"Acquired at Okinawa Institute of Science and Technology"*

The binary Mg-Pd NPs were also examined using the TEM and illustrated in Figure 3.11. In Figure 3.11 (a), the morphology of core-shell Magnesium oxide palladium NPs is shown; it can be noticed that these NPs could be subjected to some coalescence and coagulation, which could be neglected as a very small number of NPs became bigger in size than others which indicates the low possibility of coalescence phenomenon. The histogram and Gaussian fit in Figure 3.11 (b) indicates the particle size diameter is 9.2±0.8 nm, which matches the AFM results and confirms the low percentage of coalesced particles as mentioned above.

A micrograph that reveals the core-shell structure of MgO-Pd nanoparticles is shown in Figure 3.12.

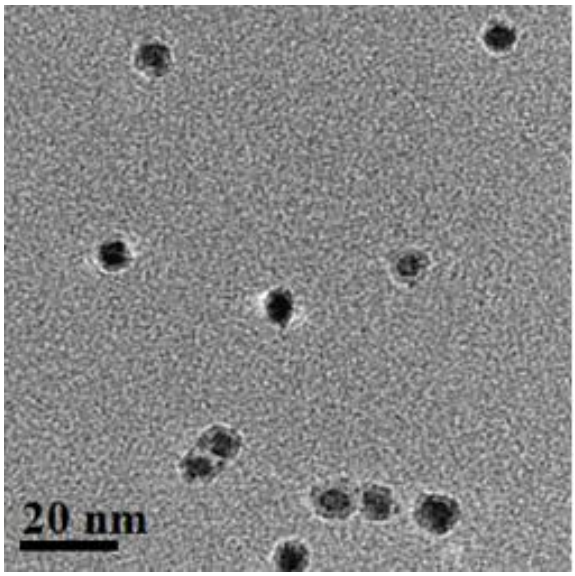

Figure 3.12 TEM image of core-shell structure MgO-Pd nanoparticles. *"Acquired at Okinawa Institute of Science and Technology"*

3.4 Surface Analysis- XPS Characterization

Elemental analysis using the X-ray photoelectron spectroscopy (XPS) for the reference and decorated electrodes' surfaces was performed before and after interaction with the MFC environment to detect whether NPs are still available or not; to indicate if they are still attached at the substrate surface after running the MFC.

The pre and post XPS characterizations of the reference electrode or the plain graphite substrate, shown in figure 3.13 and 3.14, indicate that the plain electrode has only carbon (C1s peak at 295.9 eV) and oxygen (O1s at 531.2 eV) elements onto its top surface. No magnesium oxide or metallic Pd are detected.

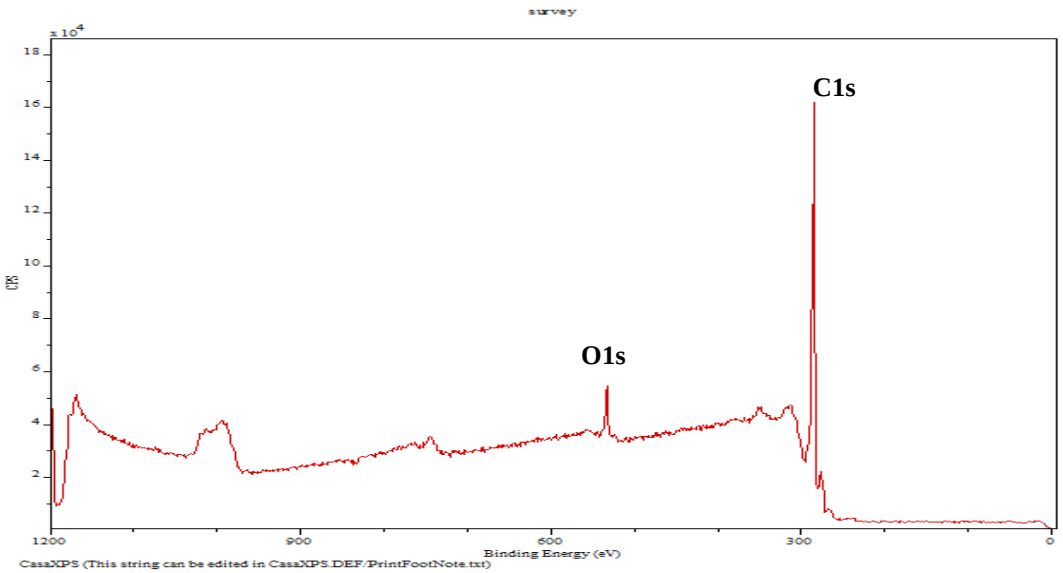

Figure 3.13: XPS spectra (survey) for plain graphite electrodes before MFC interaction insuring the presence of carbon (C1s) and oxygen (O1s). *"Acquired at Okinawa Institute of Science and Technology"*

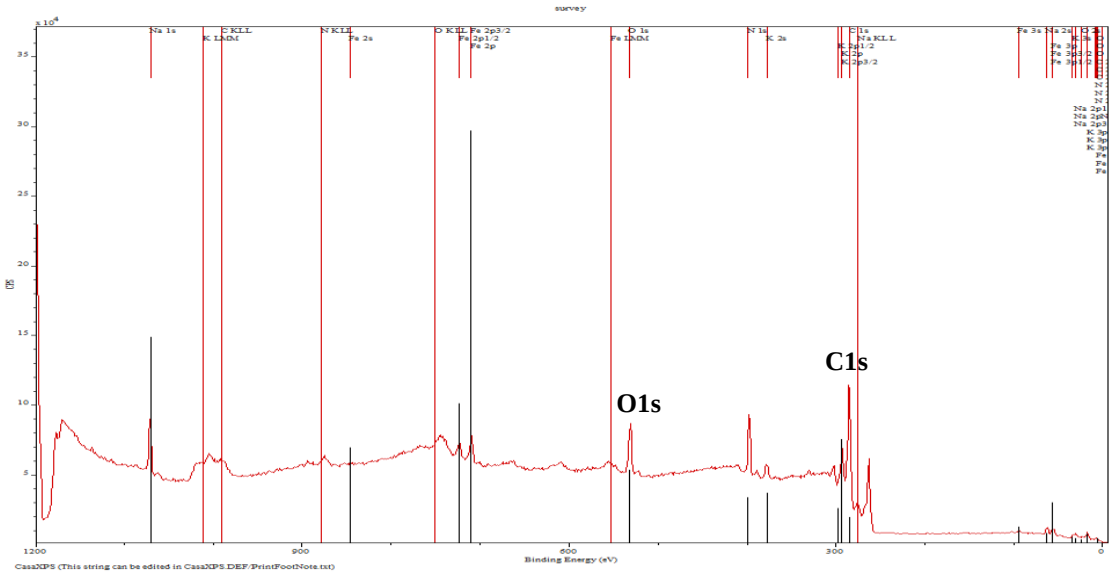

Figure 3.14: XPS spectra for plain graphite electrodes after MFC interaction where carbon (C1s) and oxygen (O1s) are detected. *"Acquired at Okinawa Institute of Science and Technology"*

Pd-decorated graphite electrodes

Pd-decorated graphite electrode XPS surface analysis is illustrated in Figure 3.15, from these spectra, the presence of the metallic Pd peaks indicates the presence of the deposited Pd NPs on the surface of graphite electrodes before and after interacting with the MFC. So after MFC running Pd NPs still exist as shown in Figure 3.16.

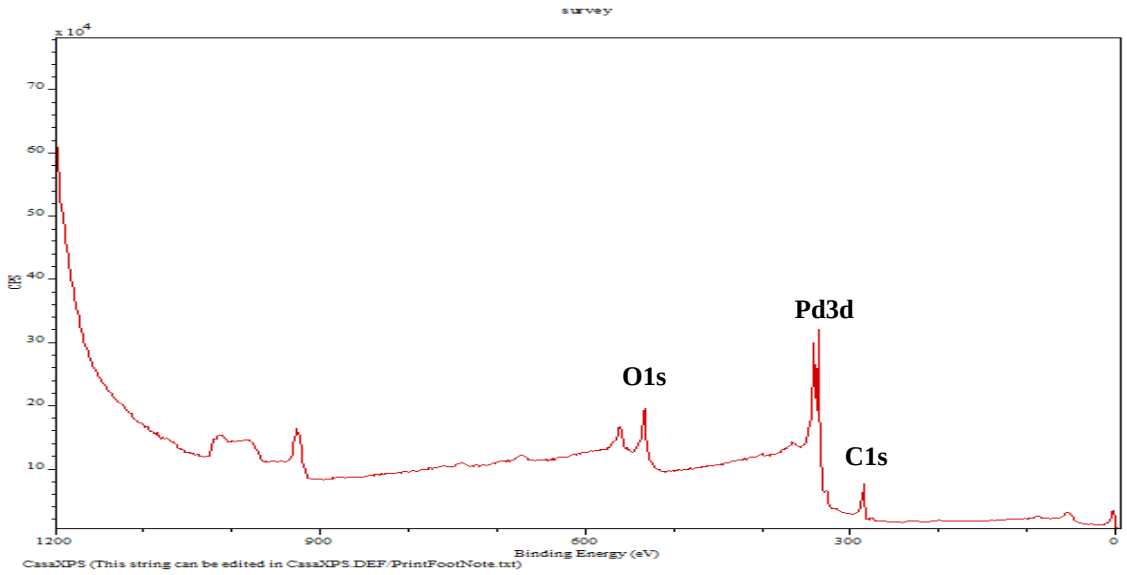

Figure 3.15: XPS spectra (survey) for Pd decorated graphite electrodes before MFC interaction indicating the presence of oxygen (O1s), carbon (C1s) and palladium (Pd3d). *"Acquired at Okinawa Institute of Science and Technology"*

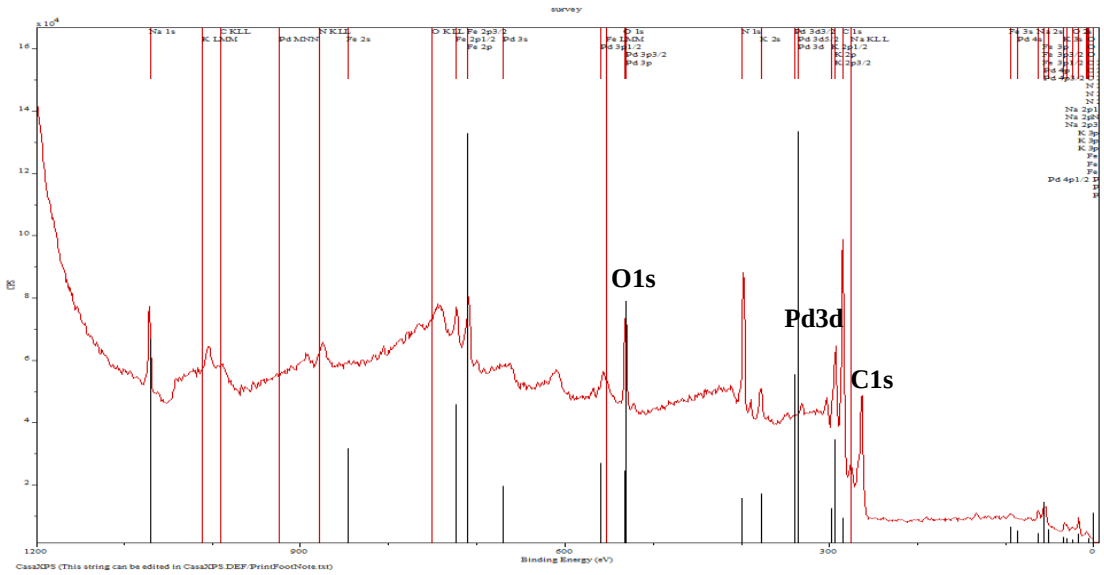

Figure 3.16: XPS spectra for Pd decorated graphite electrodes after MFC interaction. The spectra shows the existence of oxygen (O1s), carbon (C1s) and palladium (Pd3d). *"Acquired at Okinawa Institute of Science and Technology"*

MgO-Pd decorated graphite electrodes

Figures 3.17 and 3.18 show the XPS spectra for the MgO-Pd decorated graphite electrodes before and after interaction, respectively. Metallic Pd and magnesium oxide peaks are available in both spectra which confirms the presence and attachment of MgO-Pd NPs at the electrode surface before and after MFC interaction.

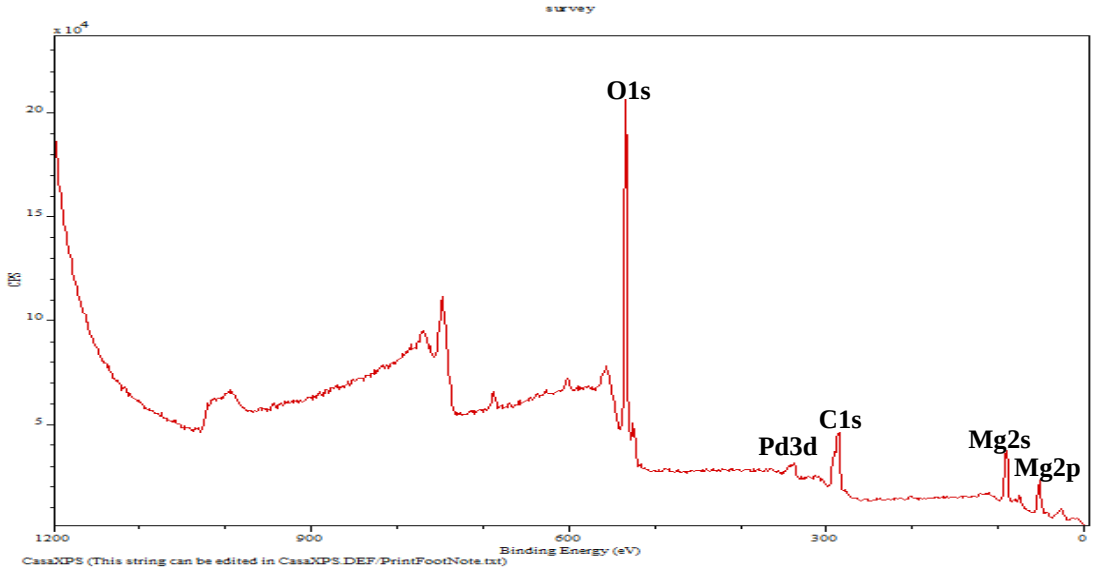

Figure 3.17: XPS spectra for MgO-Pd decorated graphite electrodes before MFC interaction which reveals the peaks of O1s, Pd3d, C1s, Mg2s and Mg2p. *"Acquired at Okinawa Institute of Science and Technology"*

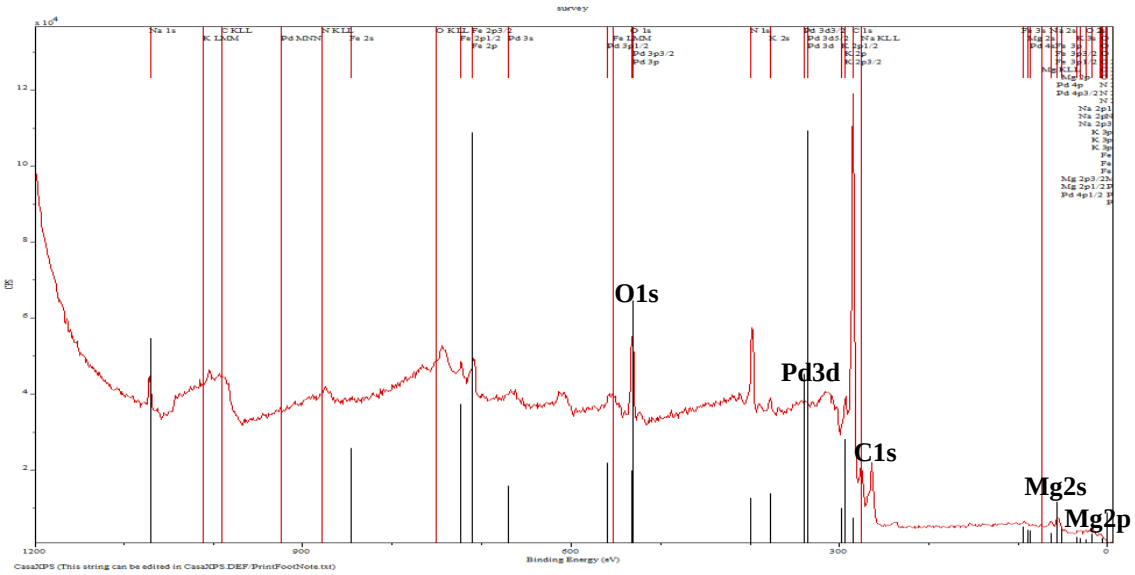

Figure 3.18: XPS spectra for MgO-Pd decorated graphite electrodes after MFC interaction indicating the presence of O1s, Pd3d, C1s, Mg2s and Mg2p peaks. *"Acquired at Okinawa Institute of Science and Technology"*

3.5 Crystallographic analysis- XRD

For the structural information about the surface of the electrodes, GI-XRD was performed on the magnesium oxide encapsulated palladium NPs decorated electrode. The XRD spectrum is shown in Figure 3.19. From this spectrum, the presence of magnesium oxide can be noticed even in small amounts; this is indicated by the peaks at 43◦ and 62◦, corresponding to the (200) and (220) planes of magnesium oxide, respectively. The highest intense peak is graphite as predicted because it's the host material or the substrate. The spectrum reflects one prominent peak at 26◦, corresponding to the (002) planes of graphite. However, Pd couldn't be detected, because they may be de-attached from the surface.

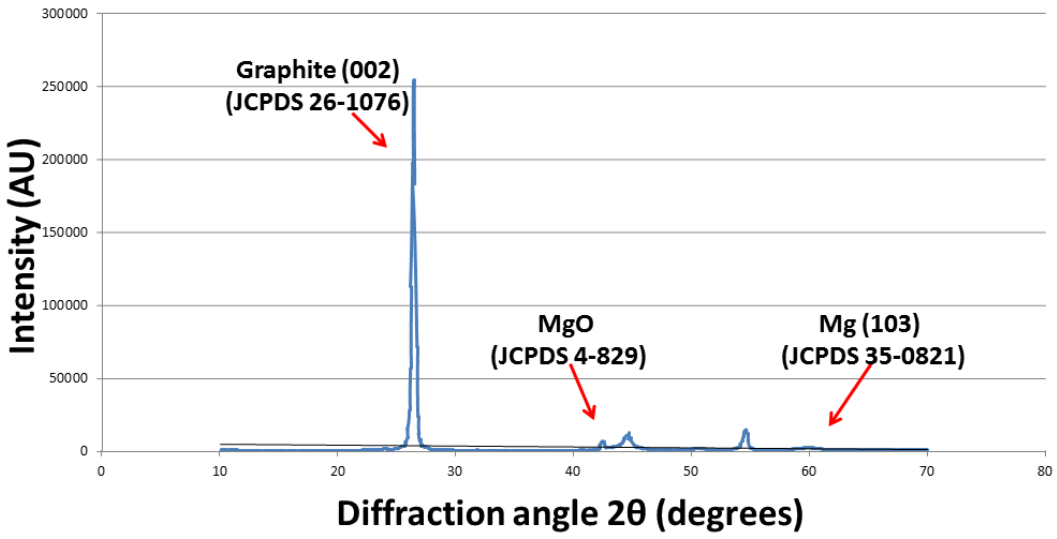

Figure 3.19: Intensity vs. diffraction angle (25-tilted_z1.7_longscan) for MgO-Pd NPs. *"Acquired at Okinawa Institute of Science and Technology"*

3.6 MFC Power Generation

The performance of MFCs with decorated and undecorated electrodes was studied; current production and power generation were investigated as functions of operating time as shown in Figure 3.20 and Figure 3.21, respectively , in order to compare and assess the efficiency of the nano-modification of MFC electrodes. Magnesium oxide encapsulated palladium nanocatalysts actually proved to enhance the produced current, which helps in developing more power and improve performance of MFC when compared to both MFCs with palladium decorated and control or undecorated electrodes. Enhanced current output was demonstrated for both NPs decorated electrodes, including the simple Pd decorated cathodes and the magnesium oxide encapsulated Pd decorated cathodes. The MgO-Pd decorated electrodes generated a maximum current density of about 34.5 $\mu A/cm^2$ after running for thirteen days, which was 2 times higher than that generated by the control electrodes (18.0 $\mu A/cm^2$). The Pd- decorated electrodes, on the other side, produced 26.4 $\mu A/cm^2$ after same running time, which was 1.3 times higher than plain graphite electrodes. However, the maximum obtained current density recorded for this design during the experiment was 41.6 $\mu A/cm^2$ generated by Pd nanoparticle decorated cathodes after 11 days of MFC running.

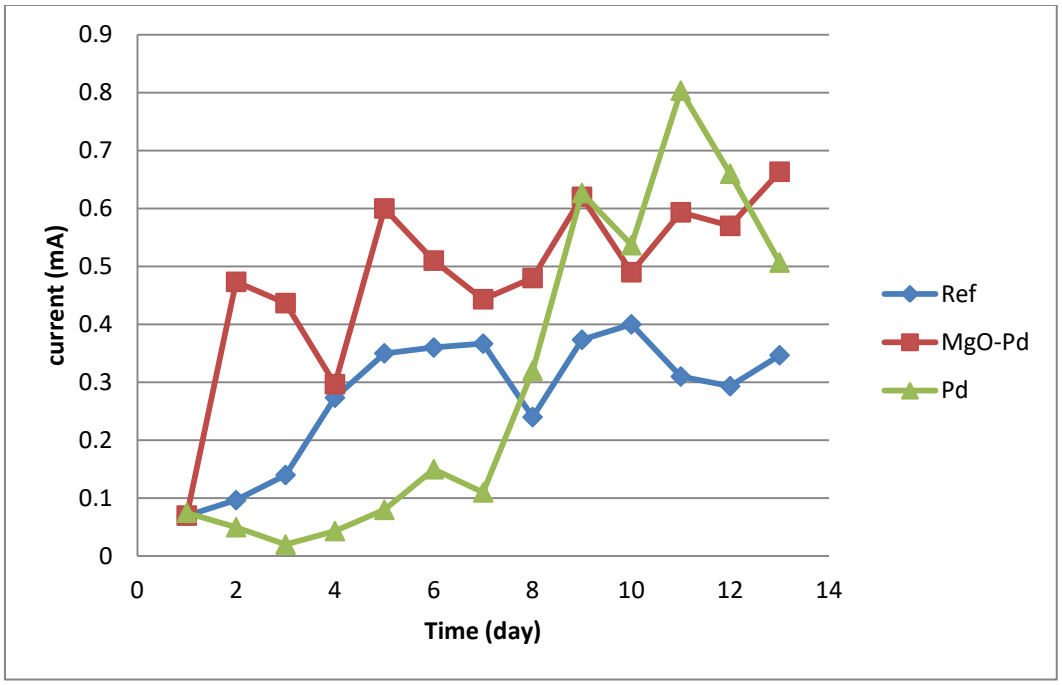

Figure 3.20: Produced current in MFCs with MgO-Pd and simple Pd decorated electrodes compared to the reference MFC with undecorated or plain electrodes. *"Acquired at Okinawa Institute of Science and Technology"*

The MgO-Pd decorated electrodes have the best and fastest enhancement in power especially in the early stages of running the MFC, which can be related to its effective core-shell nanostructure and good catalytic activity. The maximum power output recorded for the MgO-Pd core-shell NPs decorated electrodes was of about 560 µW, while that produced by Pd NPs decorated electrodes was 540 µW after 187 operating hours compared to 120µW after same running time for plain electrodes, indicating MFC with magnesium oxide encapsulated Pd NPs and conventional Pd NPs decorated electrodes produced power 4.67 and 4.5 times, respectively, higher than that produced by the control. MFCs with Pd decoration, on the other hand, were showing the worst

behavior during the early operating stages, but after nearly a week of MFC running, Pd decorated electrode started to show the improvement.

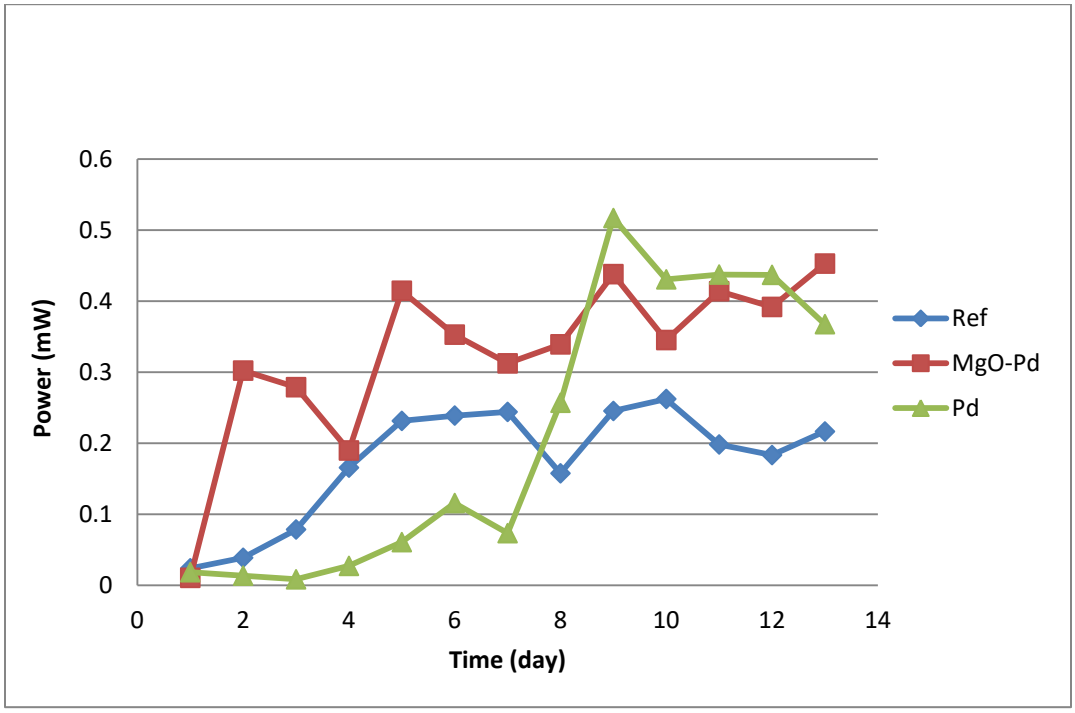

Figure 3.21: Developed power in MFCs with MgO-Pd and simple Pd decorated electrodes compared to the reference MFC with plain electrodes. *"Acquired at Okinawa Institute of Science and Technology"*

The obtained results can be explained in terms of many affecting factors. First of all, the residence time, as bacteria requires a sufficient operating time to colonize the electrode and start synthesizing the enzymes or structures responsible for electron transfer and current development. These electrodes may require more operating days in order to gain useful data that can help us reaching a good conclusion about its performance and efficiency. Furthermore, the high coverage obtained after depositing NPs onto the graphite substrate may provide some blocking sites for current production and may help

in making NPs coalesce and coagulate, especially for Pd NPs, which finally lowers the MFC performance.

The achieved enhancement doesn't seem to be stable, as the power and current versus time plots, for all decorated and plain electrodes, are going up and down, such that they are not giving a steady state signal and being fluctuating during the operating time, which is undesired in any MFC system. These unwanted fluctuations give us an indication that there's something wrong with this MFC regarding design and/or running procedure, which may be attributed to several factors. The operation time may be not sufficient as explained before and the MFC may require longer time to optimize current production, so I suggest giving this design more running time and to operate for months for example in order to estimate the best operational time. The electrodes themselves, their porosity and surface area, geometry, electrical conductivity, physical, mechanical and chemical properties and many other related factors are also critical and can significantly affect the MFC power generation. A good configuration for electrodes is necessarily needed to provide a large enough surface area for both anode and cathode; for anode to help obtaining optimal bacterial adhesion and for cathode to ensure efficient current collection. The electrolyte and the membrane have also great effects on the whole system. The electrolyte may be depleted with time and should be regularly changed and refreshed, that's why in our MFC system we changed it several times. A periodic cleaning of electrodes is necessary, because electrolyte salt crystals may be formed on the catalysts holding side of the cathode, which would result in blocking both oxygen diffusion and proton transport and subsequently leads to decreasing cathode and whole MFC efficiency. The membrane and its projected surface area are critical too, because

the membrane is the proton exchange site that ensures enhanced catalyst membrane contact and improves cathode performance. If this membrane was degraded, it would lose its functionality, so it should be checked frequently. The membrane we used in our MFC, by the way, was in a good situation and checked before assembly but it was an old one. Thus, it's better to replace it with a brand new and in a good condition one. Also, the type of microorganisms being used to harvest electricity is very important as the bacteria used from the sludge may be not active enough or died before producing considerable amount of power. Bacteria may be dead or poisoned due to the surrounding uncontrollable environment. Furthermore, bacteria feed has a great influence too, even though the standard amount of feed was used (acetate, 2 g/L), it may be insufficient for this design as bacteria should be provided with an enough feed to work efficiently and give the desired potential. So, I suggest providing different feed concentrations until it's being optimized. However, too much feed isn't recommended as it may poison the bacteria rather than activating it. pH of the system is also important but our system is well buffered so this factor isn't taken into account.

The most affecting factor in my opinion is the internal resistance of the system, which may be very high due to many reasons beside all of the above previously discussed factors. When the cell's internal resistance is high, the amount of produced current will be reduced and the generated power won't be significant. Internal resistance is highly and mainly determined by the design itself, such that electrode spacing, cell architecture and configuration, which can strongly control the internal resistance of the system. The best achievement in such works is the design and fabrication of an MFC with tiniest internal resistance in order to improve cell efficiency.

The MFC electrodes play roles in determining the cell's internal resistance and thus its performance and improvement level. However, graphite substrates were used in this design because of the material's known and widely reported good properties that are appropriate for electrodes application. They actually have good electrical conductivity that was checked before electrode material selection and assembly and high surface area as revealed by the SEM. However, some changes may be done on the electrodes such as changing its thickness and/or electrode spacing and using an alternative material with higher surface area such as carbon brush may reduce the internal resistance and help in achieving better performance. In addition, the nanomodification applied on cathodes has a strong impact on MFC performance. In this work, the used nanocatalys have approved their efficiency in improving current production and gaining an enhanced power output, which confirms the success of the novel synthesized core-shell nanostructure, which is the main goal of this research.

3.7 Electrochemical Analysis- Cyclic Voltammetry

Cyclic voltammetry testing was applied on electrolyte solution more than once; in order to indicate the system's stability and reversibility of the available electrochemical reactions, mainly redox reactions. The results demonstrated in Figure 3.22 show that the used electrolyte (potassium ferricyandie) solution was stable. The presence of the oxidation peak (positive anodic current, i_{pa}) and the reduction peak (negative cathodic current, i_{pc}) indicates the reversibility of the electrochemical redox process.

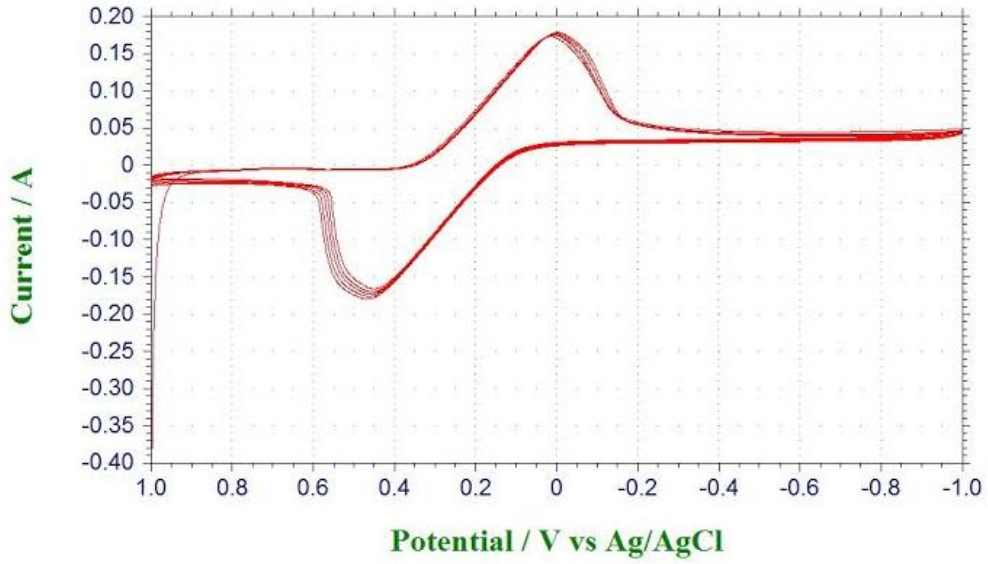

Figure 3.22: CV test results indicating the stability and reversibility of the electrochemical system involved in this research. *"Acquired at Okinawa Institute of Science and Technology"*

Chapter Four

Conclusion and Future work

4.1 Conclusions

In the present study, novel magnesium oxide (MgO) encapsulated palladium (Pd) nanoparticles and conventional Pd nanoparticles were synthesized. Sputtering of Mg and Pd from two independent neighboring targets enabled heterogeneous gas-phase condensation of nanoparticles with well-defined core-shell structure. The feasibility of this technique, equipped with the quadrupole mass filter (QMF), to produce size selected either single or binary (core-shell) nanoparticles with narrow size distribution and precise control of composition and shape was confirmed. Three selected sizes were produced in this experiment, which were 2.5 nm and 5 nm simple Pd nanoparticles and 9 nm core-shell MgO-Pd nanoparticles. These NPs were designed for the use as nanocatalysts in a microbial fuel cell to improve its performance in electricity generation.

Morphology of the nanodecorated and plain MFC electrodes was revealed using the scanning electron microscope (SEM). The images of nanoparticles showed the high density or coverage of nanoparticles and the extremely rough surfaces of the decorated electrodes compared with the plain graphite electrode's surface. High resolution imaging of the binary MgO-Pd NPs confirmed the formation of the core-shell nanostructure.

Topographical analysis was also performed using the atomic force microscope (AFM), which indicated the height of nanoparticles obtained by AFM was consistent with the QMF size selection data for both Pd and MgO-Pd nanoparticles.

Nanoparticles size distribution was also investigated using the transmission electron microscope (TEM) showing the consistency with the AFM results. High resolution TEM imaging indicated the crystallinity of the Pd NPs regardless to their size.

Surface elemental and crystallographic analysis of modified and control electrodes were also done using the X-ray photoelectron spectroscope (XPS) and the X-ray Diffraction technique (XRD), which confirmed the presence of the MgO and metallic Pd on the nanodecorated electrodes before and after MFC interaction compared to the plain graphite electrodes that lack their presence.

The surface modification of electrodes proved its efficiency in the enhancement of current and power production for the MFC system. In other words, decorating MFC cathodes with the MgO encapsulated Pd NPs lead to the generation of power 4.67 times higher than that produced by using the undecorated cathodes, while Pd nanoparticle decorated cathodes produced an amount of power 4.5 times higher relative to the plain ones.

The metal oxide (MgO) shell didn't passivate the core, instead it inhibited the sintering or coalescence of the noble core Pd nanoparticles, which could be considered as a key contributor to the improved catalytic activity of the catalysts and enhanced MFC performance. However, the exact mechanism of enhancement is still unclear.

4.2 Future Work

As a sequel to this work, I suggest developing more efficient and lower cost electrodes, which may require increasing their surface area by changing electrode geometry or selecting a new substrate material for example carbon brush instead of graphite plates

and/or using other type of nanocatalysts. I also recommend doing further deep studies regarding the nanoparticles catalytic activity in order to investigate their impact on MFC performance and understand the exact mechanism of enhancement, which can help in designing a new MFC system with optimal and most stable power output since the main challenge in brining MFC technology out of laboratories for practical applications, besides cost, is the relatively low produced current densities.

References

Alatraktchi F. Al., Zhang Y. & Angelidaki I., 2014. Nanomodification of the electrodes in microbial fuel cell: Impact of nanoparticle density on electricity production and microbial community. *Applied Energy*, Vol.116, pp. 216-222.

Alatraktchi F. Al., Zhang Y., Noori J. S. & Angelidaki I., 2012. Surface area expansion of electrodes with grass-like nanostructures and gold nanoparticles to enhance electricity generation in microbial fuel cells. *Bioresource Technology*, Vol.123, pp. 177-183.

Binning G., Quate C. F. & Gerber Ch., 1986. Atmoic Force Microscope. *Physical Review Letters*, Vol. 56, pp. 930-934.

Bonger A., Jouneau P., Thollet G., Basset D. & Gauthier C., 2007. A history of scanning electron microscopy developments: Towards "wet-STEM" imaging. *Micron*, Vol. 38, pp. 390-401.

Cassidy C., Singh V., Hawash Z., Bohra M., Kim J. & Sowwan M., 2013. Size-controlled deposition of Ag and Si nanoparticle structures with gas-aggregated sputtering. *Materials Research Society*, Vol.1546, pp. 54-60.

Chae K. J., Choi M., Ajayi F. F., Park W., Chang I. S. & Kim I. S., 2008. Mass transport through a proton exchange membrane (Nafion) in microbial fuel cells. *Energy & Fuels*, Vol. 22, pp. 169-176.

Chusuei Ch. C., D & Goodman W., 2002. X-ray Photoelectron Spectroscopy. *Encyclopedia of Physical Science and Technology*, Vol. 17., pp. 921-938.

ElMekawy A., Hegab H. M., Dominguez-Benetton X. & Pant D., 2013. Internal resistance of microfluidic microbial fuel cell: Challenges and potential opportunities. *Biosource Technology*, Vol. 142, pp. 672-682.

Fan Y., Xu Sh., Schaller R., Jiao J., Chaplen F. & Liu H., 2011. Nanoparticle decorated anodes for enhanced current generation in microbial electrochemical cells. *Biosensors and Bioelectronics*, Vol.26, pp. 1908-1912.

Gracia-Pinilla M., Martíez E., Vidaurri G. S. & Pérez-Tijerina E., 2010. Deposition of size-selected Cu nanoparticles by inert gas condensation. *Nanoscale Research Letters*, Vol.5, pp. 180-188.

Haberland H., Mall M., Moseler M., Qiang Y., Reiners T. & Thurner Y., 1994. Filling of micro-sized contact holes with copper by energetic cluster impact. *Journal of Vacuum Science & Technology*, Vol. 12, pp. 2925-2930

Jang S. S., Molinero V., Tahir & Goddard W. A., 2004. Nanophase-segregation and transport in Nafion 117 from molecular dynamics simulations: Effect of monomeric sequence. *The Journal of Physical Chemisty B*, Vol. 108, pp. 3149-3157.

Jin Z., Nackashi D., Lu W., Kittrell C. & Tour J. M., 2010. Decoration, migration, and aggregation of Palladium nanoparticles on graphene Sheets. *Chemistry of Materials*, Vol.22, pp. 5695-5699.

Kundu A., Sahu J. N., Redzwan Gh. & Hashim M. A., 2012. An overview of cathode material and catalysts suitable for generating hydrogen in microbial electrolysis cell. *International Journal of Hydrogen Energy*, Vol. 38, pp. 1745-1757.

Kuznetsova T. G., Starodubtseva M. N., Yegorenkov N. I., Chizhik S. A. & Zhdanov R. I., 2007. Atomic force microscopy probing of cell elasticity. *Micron*, Vol. 38, pp. 824-833.

Leary J. F., 2010. Nanotechnology: what is it and why is small so big?. *Canadian Journal of Ophthalmology*, Vol.45, pp. 449-455.

Lin Ch., Wu Ch., Chiu Y. & Tsai Sh., 2014. Effects of different mediators on electricity generation and microbial structure of a toluene powered microbial fuel cell. *Fuel*, Vol. 125, pp. 30-35

Logan B. E., 2010. Scaling up microbial fuel cells and other bioelectrochemical systems. *Applied Microbiology and Biotechnology*, Vol.85, pp. 1665-1671.

Ma M., Dai Y., Zou J., Wang L., Pan K. & Fu H., 2014. Synthesis of iron oxide/partly graphitized carbon composites as a high-efficiency and low-cost catalyst for microbial fuel cells. *ACS Applied Materials and Interfaces*, Vol. 6, pp. 13438-13447.

Mayoral A., Mejía-Rosales S., Mariscal M. M., Pérez-Tijerina E. & José-Yacamán M., 2010. The Co-Au interface in bimetallic nanoparticles: A high resolution STEM study". *Nanoscale - Royal Society of Chemistry*, Vol.2, pp. 2647-2651.

Mayoral A., Deepak F. L., Esparza R., Casillas G., Magen C., Perez-Tijerina E. & Jose-Yacaman M., 2012. On the structure of bimetallic noble metal nanoparticles as revealed by aberration corrected Scanning Transmission Electron Microscopy (STEM). *Micron*, Vol.43, pp. 557-564.

Meyer E., 1992. Atmoic Force Microscopy. *Progress in Surface Science*, Vol. 41, pp. 3-49.

Miller Ph. E. & Denton M. B., 1986. The Quadrupole Mass Filter: Basic operating concepts. *Journal of Chemical Education*, Vol. 63, pp. 617-620.

Pelta R. K., Vivekanandhan S., Misra M., Mohanty A. K. & Satyanarayana N., 2012. Soybean (glycine max) leaf extract based green synthesis of palladium nanoparticles. *Journal of Biomaterials and Nanobiotechnology*, Vol. 3, pp. 14-19.

Prior D. J., Bolye A. P., Brenker F., Cheadle M. C., Day A., Lopez G., Peruzzo L., Potts G. J., Reddy S., Spiess R., Timms N. E., Trimby P., Wheeler J. & Zetterstorm L., 1999. The application of electron backscatter diffraction and orientation contrast imaging in the SEM to textural problems in rocks. *American Mineralogist*, Vol. 84, pp. 1741-1759.

Qiao Y. & Li Ch. M., 2011. Nanostructured catalysts in fuel cells. *Journal of Materials Chemistry*, Vol. 21, pp. 4027-4036.

Sharma T., Reddy AL., Chandra TS., Ramaprabhu S., 2008. High power density from Pt thin film electrodes based microbial fuel cell. *Journal of Nanoscience and Nanotechnology*, Vol. 8, pp. 4132-4134

Singh V. , Cassidy C., Abild-Pedersen F., Kim J., Aranishi K., Kumar S., Lal Ch., Gspan Ch., Grogger W. & Sowwan M., 2015. Engineering high-performance Pd core-MgO porous shell nanocatalysts via heterogeneous gas-phase synthesis. *Nanoscale*, Vol. 7, pp. 13387- 13392.

Singh V. , Cassidy C., Bohra M., Galea A., Hawash Z. & Sowwan M., 2013. Surface morphology of films grown by size-selected Ta nanoparticles. *Advanced Materials Research*, Vol.647, pp. 732-737.

Singh V. , Cassidy C., Grammatikopoulos P., Djurabekova F., Nordlund K. & Sowwan M., 2014. Heterogeneous gas-phase synthesis and molecular dynamics modeling of janus and core-satellite Si-Ag nanoparticles. *The Journal of Physical Chemistry*, Vol.118, pp. 13869-13875.

Singh V., Grammatikopoulos P., Cassidy C., Benelmekki M., Bohra M., Hawash Z., Baughman K. W. & Sowwan M., 2014. Assembly of tantalum porous films with graded oxidation profile from size-selected nanoparticles. *Journal of Nanoparticle Research*, Vol.16, pp. 2373-2377.

Stenina I. A., Sistat Ph., Rebrov A. I., Pourcelly G. & Yaroslavtsev A. B., 2004. Ion mobility in Nafion-117 membranes. *Desalination*, Vol. 170, pp. 49-57.

Virdis B., Rabaey K., Yuan Z., Rozendal R. A. & Keller J., 2009. Electron fluxes in a microbial fuel cell performing carbon and nitrogen removal. *Environmental Science & Technology*, Vol. 43, pp. 5144-5149.

Virdis B., Rabaey K., Rozendal R. A., Yuan Z. & Keller J., 2010. Simultaneous nitrification, denitrification and carbon removal in microbial fuel cells. *Water Research*, Vol. 44, pp. 2970-2980.

Wang Z. L., 2000. Transmission Electron Microscopy of Shape-Controlled Nanocrystals and Their Assemblies. *The Journal of Physical Chemistry*, Vol. 104, pp. 1153-1175.

Wang H., Park J. & Ren Z. J., 2015. Practical Energy Harvesting for Microbial Fuel Cells: A Review. *Environmental Science and Technology*, Vol. 49, pp. 3267-3277.

Wei J., Liang P. & Huang X., 2011. Recent Progress in Electrodes for Microbial Fuel Cells. *Bioresource Technology*, Vol.102, pp. 9335-9344.

Wei L., Han H. & Shen J., 2012. Effects of cathodic electron acceptors and potassium ferricyanide concentrations on the performance of microbial fuel cell. *International Journal of Hydrogen Energy*, Vol. 37, pp. 12980-12986.

Wen Z., Ci S., Mao Sh., Cui Sh., Lu G., Yu K., Luo Sh., He Z. & Chen J., 2013. TiO_2 nanoparticles-decorated carbon nanotubes for significantly improved bioelectricity generation in microbial fuel cells. *Journal of Power Sources*, Vol. 234, pp. 100-106.

Xu Sh., Liu H., Fan Y., Schaller R., Jiao J. & Chaplen F., 2012. Enhanced performance and mechanism study of microbial electrolysis cells using Fe nanoparticle-decorated anodes. *Applied Microbiology and Biotechnology*, Vol.93, pp. 871-880.

Yang D., Velamakanni A., Bozoklu G., Park S., Stoller M., Piner R. D., Stankovich S., Jung I., Field D. A., Ventrice Jr. C. A. & Ruoff R. S., 2009. Chemical analysis of grapheme oxide films after heat and chemical treatments by X-ray photoelectron and Micro-Raman Spectroscopy. *Carbon*, Vol. 47, pp. 145-152.

Yuan Y., Ahmed J. & Kim S., 2011. Polyaniline/carbon black composite-supported iron phthalocyanine as an oxygen reduction catalyst for microbial fuel cells. *Journal of Power Sources*, Vol. 196, pp. 1103-1106.

http://www.nanoscience.com/products/sem/technology-overview/how-sem-works/,

27/7/2015

htt://wpww.youtube.com/watch?v=RNJKfIj8WlQ, 3/8/2015

http://www.mantisdeposition.com/nanoparticlegenerators.html, 28/3/2016

http://www.shimadzu.com/an/lcms/support/intro/lib/lctalk/61/61intro.html, 12/4/2016

http://batteryblog.ca/2010/06/lithium-ion-anode-materials-ordered-and-disordered-carbon, 12/3/2017

http://electrons.wikidot.com/x-ray-diffraction-and-bragg-s-law, 12/3/2017

https://www.researchgate.net/figure/6699273_fig6_Fig-8-A-schematic-of-a-quadrupole-mass-filter-Resonant-ions-will-travel-down-through, 5/8/2017

جزيئات البلاديوم المغلف بأكسيد المغنيسيوم كمحفزات نانية في أقطاب خلايا الوقود الميكروبية

إعداد: رهام وليد محمد مظفر

إشراف: د. مخلص صوان

ملخص

تم في هذه الدراسة تصميم و تصنيع جسيمات نانية غير مألوفة من البلاديوم المحاط بغلاف من أكسيد المغنيسيوم (MgO-Pd Nanoparticles) لتحفيز و تحسين أداء أقطاب خلايا الوقود الميكروبية. أنتجت هذه الجسيمات بطريقة يسهل التحكم بها من خلال دمج طريقتي الترسيب الفيزيائي للبخار مع تجميع الغاز(PVD-GA)، حيث تمت تصفية هذه الجزيئات على أساس حجمها بوساطة فلتر الكتلة رباعي الأقطاب (QMF) فكان معدل طول القطر9 نانومتر في جزيئات البلاديوم المغلفة بالأكسيد و 2.5 نانومتر و 5 نانومتر في جزيئات البلاديوم المجرد.

و تم الترسيب على أسطح الأقطاب السالبة (المهبط) لدراسة تأثيرالجسيمات النانية على أداء الخلية من حيث إنتاجها للطاقة الكهربائية. و قد تبين من نتائج الدراسة أن وجود المحفزات النانية التي سبق ذكرها على أسطح الأقطاب أدى إلى تحسن ملحوظ في قدرة الخلية على إنتاج الطاقة؛ حيث أنتجت الخلية ذات المهبط المعدل بجزيئات MgO-Pd وPd المجرد طاقة أفضل 4.67 مرات و 5 مرات ،على الترتيب، مقارنة بتلك المنتجة من قبل الخلية ذات الأقطاب الخالية من الجزيئات النانية.

و قد تم استخدام المجهر الإلكتروني الماسح (SEM) و مجهر القوى الذرية (AFM) و المجهر الإلكتروني الماسح النافذ (TEM) بهدف دراسة و تحليل سطح و تضاريس هذه الجزيئات التي بينت التوافق مع النتائج المستخلصة من فلترة الجزيئات باستخدام QMF. كما و أثبت وجود التركيب المطلوب للجسميات النانية MgO-Pd حيث وضحت الصور وجود البلاديوم في المركز والأكسيد كغلاف خارجي محيط به.

و خضعت أيضاً أسطح الجرافيت المعدلة لتحاليل أخرى لإظهار التركيب الكيميائي قبل و بعد استخدامها كأقطاب في الخلية وذلك باستخدام مطيافية الأشعة السينية بالإلكترون الضوئي (XPS) و تقنية حيود الأشعة السينية بورود مماسي (Grazing incidence XRD). و قد أثبتت نتائج هذه التحاليل وجود كلاً من معدن البلاديوم و أكسيد المغنيسيوم قبل و بعد تشغيل الخلية.